Quaternary Science Reviews 221 (2019) 105897

Contents lists available at ScienceDirect

Quaternary Science Reviews

journal homepage: www.elsevier.com/locate/quascirev

Timing of the local last glacial maximum in Terra Nova Bay, Antarctica defined by cosmogenic dating

Hyun Hee Rhee [a, c], Min Kyung Lee [b], Yeong Bae Seong [a, *], Seongchan Hong [a], Jae Il Lee [b], Kyu-Cheul Yoo [b], Byung Yong Yu [c]

[a] Department of Geography, Korea University, Seoul 02841, South Korea
[b] Division of Polar Paleoenvironment, Korea Polar Research Institute, Incheon 21990, South Korea
[c] AMS Laboratory, Korea Institute of Science and Technology, Seoul 02792, South Korea

A R T I C L E I N F O

Article history:
Received 22 April 2019
Received in revised form
16 August 2019
Accepted 21 August 2019
Available online 28 August 2019

A B S T R A C T

The Jangbogo Hills are erratic-covered landforms consisting of a series of benches that are parallel to the length of Campbell Glacier, northern Victoria Land, Antarctica. We sampled 41 erratic cobbles from six benches to reveal the exposure times of glacier erratics using in situ ^{10}Be and ^{26}Al. The erratics from the upper three benches yield exposure ages older than Marine Isotope Stage (MIS) 4, with most exposed since MIS 5. However, the lower three benches exhibit tight clusters of exposure ages that range from MIS 3 to the Holocene. Campbell Glacier underwent rapid downwasting during MIS 5, centered at 98.3 ka from its maximum position at the penultimate glacial maximum (PGM). This downwasting continued throughout the last glacial period, with a potential minor stagnation around a bench (~90 m asl) between 35.4 and 17.0 ka. Our cosmogenic nuclides surface exposure dating results highlight three important points concerning the glacial history of Terra Nova Bay since the penultimate glacial maximum (PGM) in northern Victoria Land, Antarctica: 1) Campbell Glacier was thicker at the PGM than at the global last glacial maximum (LGM); 2) the local LGM occurred during MIS 4; and 3) the extent of Campbell Glacier during the global LGM (90 m) was much smaller than previously assumed (300–400 m). Hence, the previous view that the local LGM (MIS 4) in Victoria Land, Antarctica was synchronous with the global LGM (MIS 2) should be treated with caution.

1. Introduction

The global last glacial maximum (LGM) has been intensively studied to reveal the magnitude and timing of ice storage, sea level changes, and feedbacks on climate and biological changes (CLIMAP Project Members, 1981; Hughes et al., 2013), attracting considerable attention across the Earth sciences. The LGM technically represents the thickest ice (or ice sheet) period or environment, but it has been widely used as the coldest or lowest sea-level period based on several proxy studies. Many dating techniques successfully determined the period and extent of the LGM using proxies from ice cores, marine sediment cores, and glacial landforms (Hughes et al., 2013). The ice sheets reached their maximum extent during the LGM, ranging from 26.5 to 19 ka, and global sea level was at its minimum (Clark et al., 2009).

The timing and extent of the maximum glaciation in many regions is still poorly defined and may vary from one region to the next due to the various responses of ice masses in different regions to local climatic conditions. The local last glacial maximum (lLGM) was therefore proposed to address the local response to climatic changes as opposed to glacier advances that occur during the global Last Glacial Maximum (gLGM) that may not be the most extensive (Smith et al., 2005). There is a general consensus regarding the timing of the penultimate glacial maximum (PGM; *i.e.* MIS 6), but its extent versus that of the LGM is still debated. For example, the PGM ice was more extensive than the LGM ice in Eurasia, but the Laurentide Ice Sheet in North America generally reached its maximum limit during the LGM, with the exception of some protrusions of older till (Rohling et al., 2017).

Cosmogenic nuclide dating techniques (^{3}He, ^{10}Be, ^{14}C, ^{20}Ne, ^{21}Ne, and ^{26}Al) have targeted many ice-free but formerly glaciated areas across the most glaciated area, Antarctica, to reveal the glacier changes associated with climatic changes. These ice-free areas are

* Corresponding author.
E-mail address: ybseong@korea.ac.kr (Y.B. Seong).

https://doi.org/10.1016/j.quascirev.2019.105897

concentrated on the Antarctic Peninsula and throughout the Transantarctic Mountains (TAM). These glaciers on Victoria Land adjacent to the Ross Ice Shelf in the TAM, currently drain the East Antarctic Ice Sheet into the Ross Sea but they drained into the Ross Ice Shelf in the past (Baroni et al., 2005). Many studies have investigated the glacier histories from the Dry Valleys in southern Victoria Land, and from Deep Freeze Range in northern Victoria Land, where they not only revealed that the Antarctic glacier transition from a warm-to cold-based glacier environment occurred several million years ago (Fig. 1; Nishiizumi et al., 1991; Ivy-Ochs et al., 1995; Schäfer et al., 1999; Oberholzer et al., 2003; Oberholzer et al., 2008; Strasky et al., 2009; Di Nicola et al., 2009; Di Nicola et al., 2012), but they also attempted to constrain the timing and extent of glaciation during the LGM (Mackintosh et al., 2007; Lilly et al., 2010; Joy et al., 2017; Goehring et al., 2019).

Here, we present the first comprehensive Quaternary glacial history of Terra Nova Bay (TNB) in Antarctica. We sampled erratic cobbles from previously glacier-covered benches near Campbell Glacier, Terra Nova Bay, to determine exposure ages using the terrestrial cosmogenic nuclides ^{10}Be and ^{26}Al to construct the detailed Quaternary glacial history of Campbell Glacier. Our results are particularly pertinent to the understanding of the timing and ice extent of the lLGM in Victoria Land.

2. Study area

Campbell glacier is sourced from dozens of local mountain glaciers that drain the Deep Freeze Range and Southern Cross Mountains (Fig. 2A). Archambault Ridge, which is currently in the upglacier area of Campbell Glacier, was exposed during at least 7−5 Ma (Di Nicola et al., 2012). Campbell Glacier changed from a warm-to cold-based glacier during this period of 7−5 Ma, when its maximum thickness was attained and there was limited subglacial erosion. The other glaciers draining into TNB (e.g., Priestley, Reeves, Larsen, Hollingsworth, and David) flow into Nansen Ice Shelf and Drygalski Ice Tongue. Only Campbell Glacier drains into TNB as Campbell Ice Tongue, flowing between Shield Nunatak and the northern part of the Northern Foothills.

An unnamed spear-shaped landmass extends northward between Browning Pass and Campbell Ice Tongue at the northern part

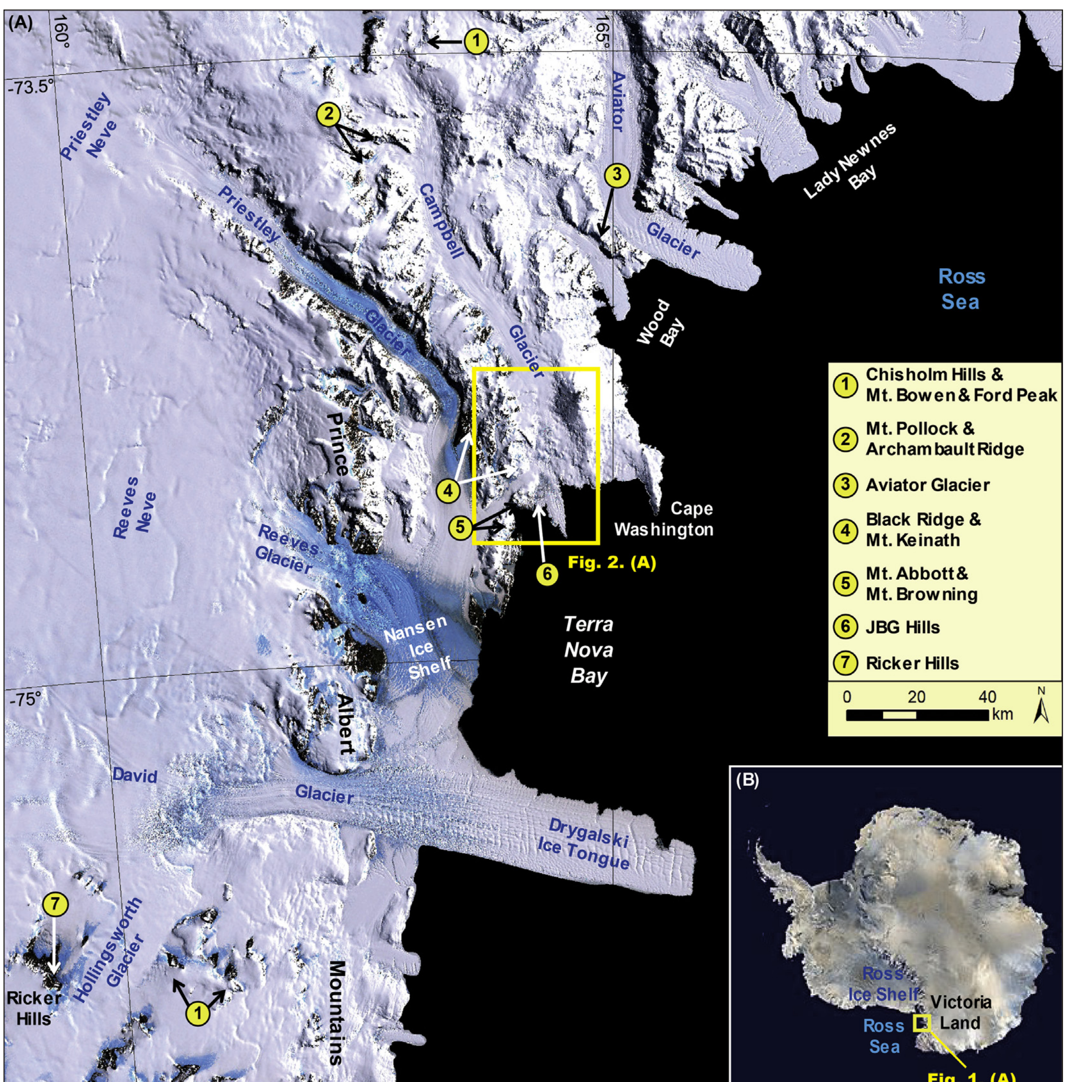

Fig. 1. (A) Landsat Image Mosaic of Antarctica (LIMA) of Terra Nova Bay, Ross Sea, showing the locations of the present and previous studies of glacier change. ① Oberholzer et al. (2008); ② Di Nicola et al. (2012); ③ Goehring et al. (2019); ④ Oberholzer et al. (2003); ⑤ Di Nicola et al. (2009); ⑥ the present study area at Jangbogo Hills on the northwestern part of Terra Nova Bay; and ⑦ Strasky et al. (2009). (B) Location of Terra Nova Bay relative to Antarctica.

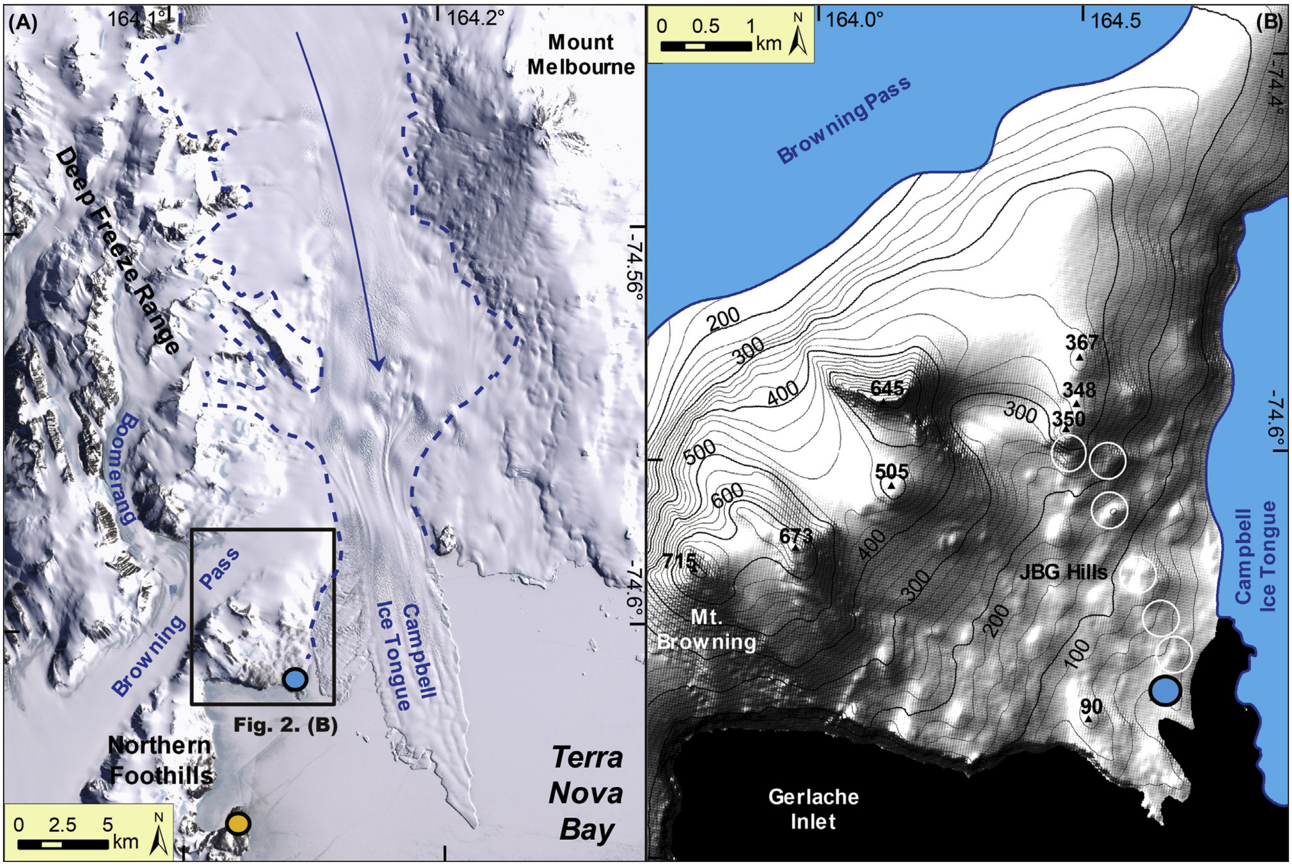

Fig. 2. (A) LIMA image of the terminal region of Campbell Glacier. Campbell Glacier flows northward from Gair Mesa, draining local mountain glaciers from the Deep Freeze Range and Southern Cross Mountains. Campbell Ice Tongue flows directly into TNB. The present study area, JBG Hills, parallels Campbell Ice Tongue to the west. The orange and blue circles indicate Mario Zucchelli (Italy) and Jang Bogo (Korea) stations, respectively. (B) Hillshade relief map of the northern part of the Northern Foothills. The slopes in the study area show irregular convex mounds that consist of erratics. The blue areas indicate ice cover and white circles are locations of sampled benches. (For interpretation of the references to colour in this figure legend, the reader is referred to the Web version of this article.)

of the Northern Foothills in TNB (Fig. 2B). The northern and southern slopes of this landmass are divided by a discontinuous ridge that consists of Mt. Browning (715 m), unnamed peaks (673 and 645 m), and Jangbogo (JBG Hills; 348–367 m). Deeply carved U-shaped valleys have developed between each peak due to the debuttressing of local ice. The southern sides of these peaks exhibit steep upper slopes and gentle lower slopes. The lower northern slope of Browning Pass is almost entirely covered by glaciers to >100 m above sea level (asl), whereas the southern slope is entirely exposed due to the lowering of Campbell Glacier. The bedrock, which is rarely exposed because of debris cover, is composed of diorite, gneiss, and granite (Kim et al., 2018). The southern slope is overlain by sparsely developed convex moraine mounds that are covered with erratics. These moraines primarily contain granitic erratics, with gneiss, quartzite, and lesser amounts of volcanic rock.

Intense summertime snowfall covers the study area with light snowpack (25.2 cm; Han et al., 2017) that is easily sublimated by strong, dry winds from the glaciated area and increased temperatures (>0 °C) during midsummer, such that our study area is largely snow-free. This light snowpack has a negligible impact on the production of cosmogenic nuclides, such that the shielding effects (<1%) due to snow cover can be ignored (Fabel and Harbor, 1999; Di Nicola et al., 2009). The terminus of Campbell Ice Tongue retreated ~4.4 km between 1984 and 2016, and flowed at a rate of ~0.3 km a^{-1} between 2011 and 2016, but it is now stuck at the lateral margin (Google Earth, 1984–2016). Ice growth is commonly observed between the terrestrial edge of the study area and Campbell Ice Tongue (Fig. 2B).

3. Method

3.1. Sampling strategy

We used the Reference Elevation Model of Antarctica (REMA; Howat et al., 2019) to produce a topographic hillshade map for distinguishing the moraine sequences (Fig. 2B). We selected six moraine mounds with similar elevations or distance intervals (Fig. 3A). Bench A (305 m above sea level [asl]) was just beneath the ridge running parallel to the direction of Campbell Glacier, with a convex moraine, and benches B (235 m asl) and C (159 m asl) were selected due to their concavity (Fig. 3B). Benches D (90 m asl), E (41 m asl), and F (33 m asl) have almost flat steps with gentler slopes than the upper three benches (Fig. 3C). Although the lower three benches do not necessarily cover different altitude intervals, the distance intervals between these benches are distinct, such that they are different moraine sequences.

We focused our sampling strategy on avoiding nuclide inheritance, one of the main challenges of cosmogenic nuclide dating in Antarctica (Balco and Schaefer, 2013). Inherited cosmogenic nuclides can result from supraglacial pre-exposure, multiple exposures, and incorporation of older drifted materials (Ivy-Ochs et al., 2007; Di Nicola et al., 2009). Our sampling strategies were designed to minimize inheritances. Several other sources of inheritance still exist which could not be considered during our fieldwork. Erratic

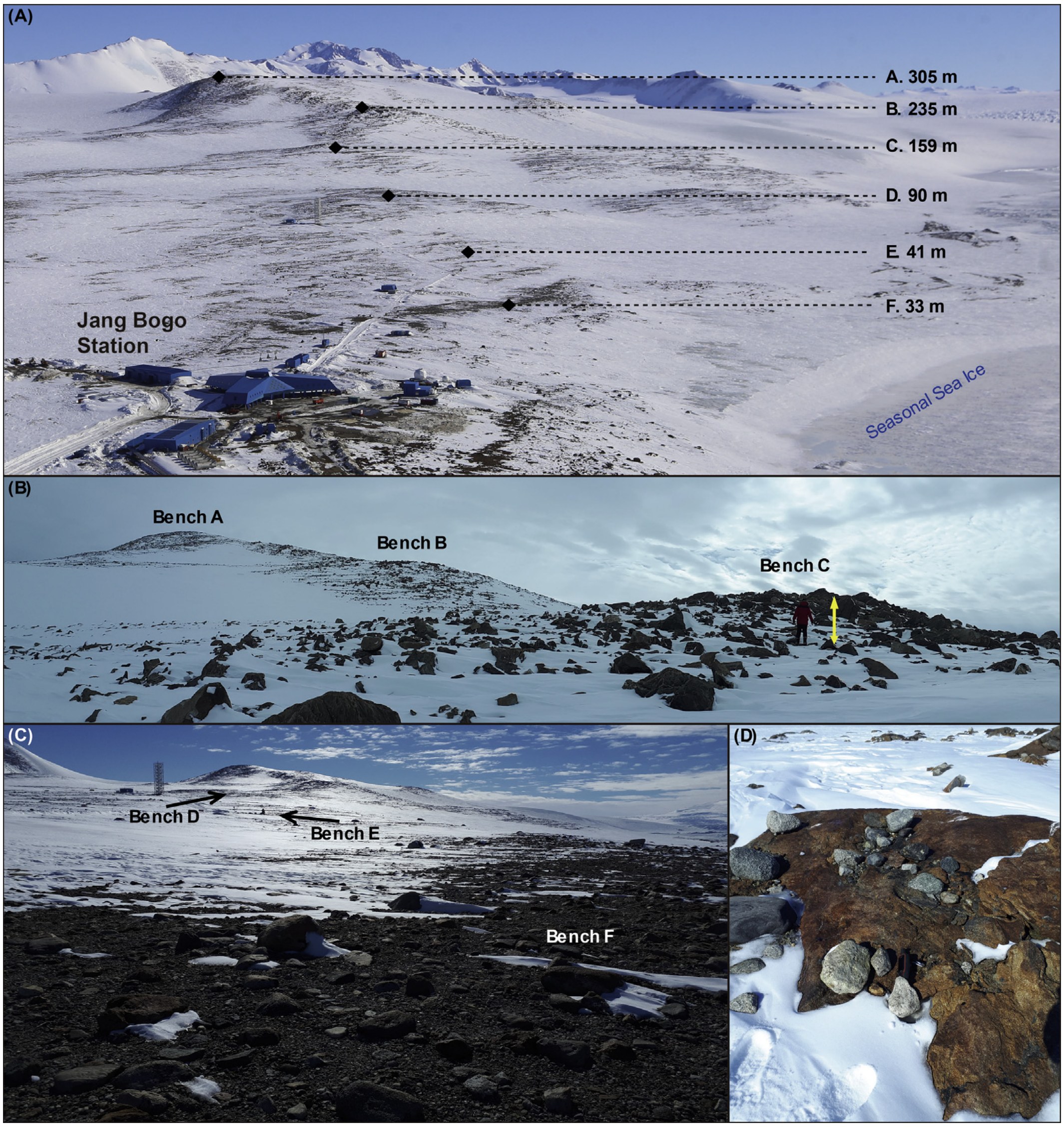

Fig. 3. Views of the study area (A) and sampling sites (B–D). (A) Oblique aerial photograph of the study area that shows the six sampled benches. (B) Upper three benches (A–C), which show convex mounds and are almost entirely covered by erratic boulders. A person (yellow arrow) is shown for scale. (C) Lower three benches (D–F), which are subtle but distinct ridges compared to the other snow-covered areas. (D) Example of a sample location on bench E. Each sample was collected from high and large boulders on the flat section of a given bench to minimize disturbance from local slope processes. Bullet-shaped cobbles, which were assumed to be transported via subglacial processes, were selected to minimize the inherited ^{10}Be and ^{26}Al concentrations. Cobbles with lithologies that were different from the bedrock were also sampled. (For interpretation of the references to colour in this figure legend, the reader is referred to the Web version of this article.)

boulders and cobbles are common across the study area which we targeted because they are more likely to experience simple exposure (Balco and Schaefer, 2013; Jeong et al., 2018). Each sample was collected from either a high and stably standing large boulder that was not disturbed by local slope processes (Fig. 3D). Convex mounded moraines were the primary targets for this sampling strategy because they are less likely to have boulders and cobbles transported by local slope processes. Cobbles with lithologies different from that of the local bedrock and that had abraded edges were also considered to make a distinction between in situ weathered fragments. Angular pseudo-erratic cobbles were easily found with their well preserved jigsaw pattern due to the little fluvial and eolian transportation. Bullet-shaped cobbles polished via subglacial processes were selected to prevent pseudo-erratics and supraglacial inheritance which may overestimate the real timing of deglaciation.

3.2. Analytical methods

We extracted in situ ^{10}Be and ^{26}Al from the same quartz samples for isotopic analysis. Continuously exposed quartz should plot within the steady-state erosion zone of the two-isotope ^{10}Be–$^{26}Al/^{10}Be$ plot (Lal, 1991), whereas a burial event will yield different isotopic ratios over time due to the different half-lives of the decaying isotopes. Samples that have undergone multiple exposures and burial by ice generally possess smaller $^{26}Al/^{10}Be$ ratios than those with simple exposure in the two-isotope plot (Lal, 1991; Gosse and Phillips, 2001, Fig. 4B) and should be treated as outliers for each bench. It is not straightforward to determine complex exposure history for samples younger than ~200 kyr due to the decreasing gap between two isotopes' half-lives (Lal, 1991; Gosse and Phillips, 2001). However, it was still effective for finding lack of a burial with 50 ka exposed samples on East Antarctica (Lilly

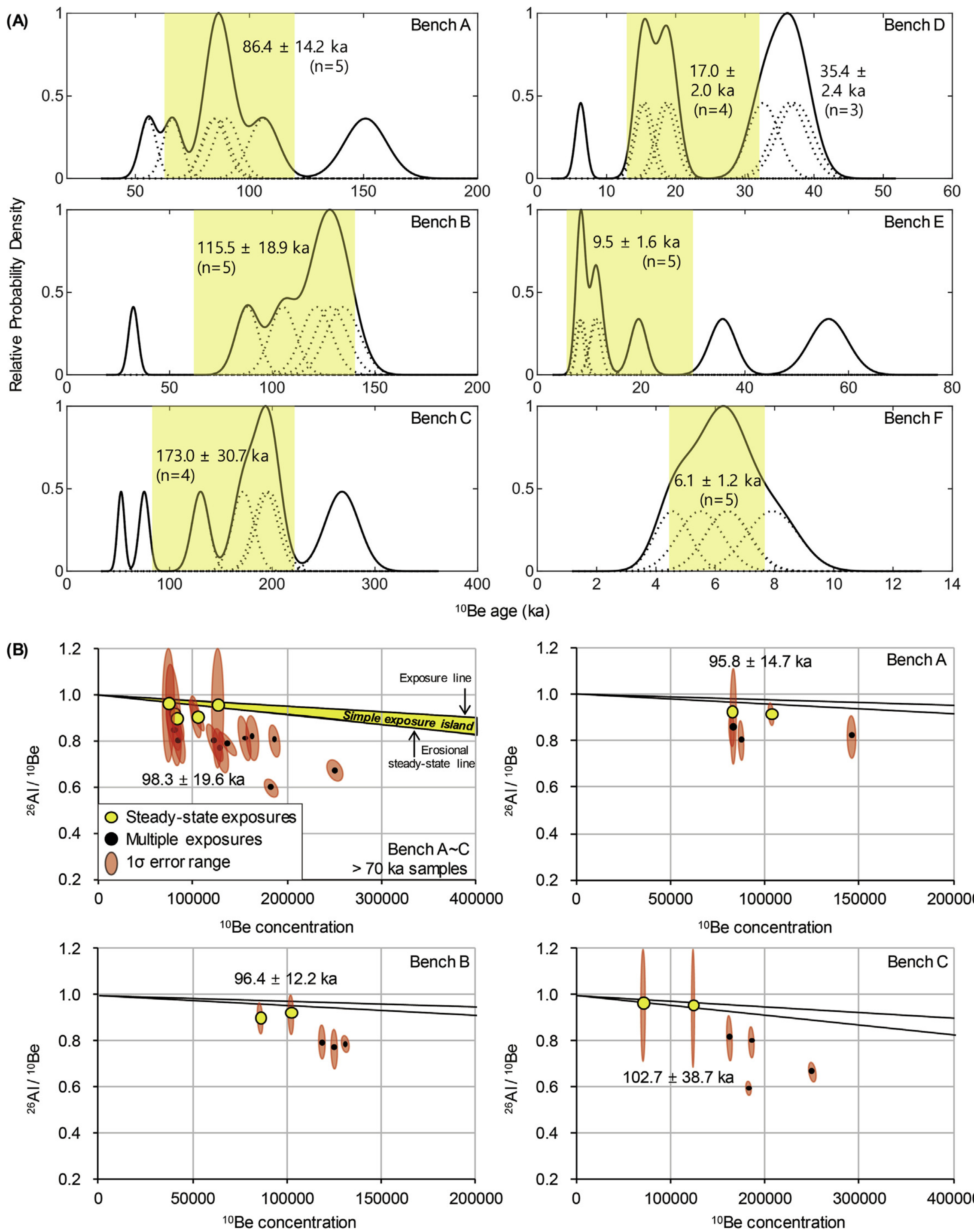

Fig. 4. (A) Relative probability density plots for each bench and 95% confidence interval with sample age distribution in yellow ranges. Values are mean ages and distributions of inlier samples. Lower three benches (D–F) used statistical method such as SEM and PDF to identify outliers and effective exposure ages. Dashed curves show individual samples. (B) Two-isotope plot used to infer the multiple-exposure history of samples with older apparent exposure ages (>MIS 4) from the upper three benches (A–C). These plots were calculated with CRONUS-Earth online calculator 3.0 of Balco et al. (2008) with scaling factors of Stone (2000). The yellow circles indicate samples that were continuously exposed. The black circles indicate samples with multiple-exposure and the red oval is one sigma. (For interpretation of the references to colour in this figure legend, the reader is referred to the Web version of this article.)

et al., 2010). In this study, we targeted only samples which have ^{10}Be ages older than 70 ka.

We employed multiple statistical methods to identify the various exposure histories via the analysis of multiple in situ cosmogenic nuclides, which assisted in distinguishing the representative or effective ages at each bench. We primarily considered batched (6–8) samples within the 2σ confidence level of the standard error of the mean (SEM) for the statistical methods. Standard deviation (SD) is generally used as an accuracy of the mean from its sample data, and SEM is a SD of those sample data sets which produces sampling distributions (Douglas, 2008). The SEM is used for defining the confidence level based on the standard deviation of the sampling distribution, such as the age results from the collected samples at each bench. Either younger or older than clustering ranges of 95% confidence level at each bench were considered as outliers. The probability density function (Camel Plot) was also used to obtain an effective age cluster for each bench although it provides only an aid to eye. The relative probabilities for each sample were then plotted together with their own Gaussian kernel, showing the frequency distribution of ages of samples and clustered area. They represent the relative degree of clustering and their age ranges, which allow the inlier samples to be distinguished from the age-scattered samples by isolating or combining the outliers.

3.3. *In situ ^{10}Be and ^{26}Al*

Forty-one samples were processed at the Geochronology Laboratory, Korea University, following the method outlined by Seong et al. (2016), which is modified from the procedure of Kohl and Nishiizumi (1992). All samples were pulverized using an iron mortar, sieved to medium sand (250–500 μm), and chemically treated to remove all particles except pure quartz. The samples were leached with either 3 or 1% hydrofluoric acid (HF)/nitric acid (HNO_3) solution alternating in either in an ultra-sonic bath or on heated rollers. This process was repeated several times to yield pure quartz grains. Then, ^{9}Be carrier solution was added into the samples. The ^{9}Be spike and ^{10}Be from the dissolved quartz were mixed in a high-concentration hydrofluoric acid/nitric acid solution to form beryllium nitride. The pure quartz contains ^{27}Al, which we analyzed by inductively coupled plasma–atomic emission spectroscopy (ICP–AES) at the Korea Basic Science Institute, Seoul, Korea. Perchloric acid was used to remove F and prevent Be loss via the formation of beryllium fluoride. Hydrochloric acid was used to generate mixed Be–Al samples in chloride form, which were then passed through anion- and cation-exchange columns. Be and Al were separately collected in chloride form, neutralized, and precipitated as hydroxide gels with $NH_{3(aq)}$. These gels were then dried in a quartz crucible and calcined at high temperature to yield their oxide forms. The oxidized materials were ground into fine powders, which were then mixed with niobium and silver powder. Each powder was pressed in either an aluminum target for BeO or a copper target for Al_2O_3., and measured with a 6 MV accelerator mass spectrometer (AMS) at the Korea Institute of Science and Technology, Seoul, Korea.

The measured ^{10}Be/^{9}Be and ^{26}Al/^{27}Al ratios were normalized to standard samples (Nishiizumi et al., 2007). Concentration of rare isotopes were calculated with normalized ratio to stable isotope concentration. Process blanks were deducted from the measured blank samples using AMS and ICP–AES. The calculated ^{10}Be and ^{26}Al concentrations, along with key sample information (coordinates, elevation, thickness, density, and shielding factor), were used to calculate the exposure ages via the CRONUS-Earth online exposure age calculator V 3.0 (Balco et al., 2008), with Stone's scaling factors (Stone, 2000).

4. Results

The samples from the three upper benches (A–C) and the three lower benches (D–F) yield markedly different ^{10}Be exposure ages (Fig. 4A; Table 1). The upper bench samples exhibit much older ages that are primarily Marine Isotope Stage (MIS) 5 or older, with a few MIS 3 ages. Benches A and B yield mainly MIS 5 ages, with a few MIS 6 and younger MIS 4 and 3 ages. Bench C yields the largest scatter in ^{10}Be exposure ages, from MIS 8 to MIS 3.

The lower bench samples exhibit contrasting ages to the upper bench samples that are younger than MIS 4 (Fig. 4A). Most samples are clustered on MIS 3, late MIS 2 and the Holocene. The bench D samples have strong bimodal age distributions with peaks coinciding with late MIS 3 and MIS 2. The bench E samples yield mainly MIS 1 ages, with minor clusters during MIS 3 and 2. The bench F samples exhibit the tightest age cluster during the middle Holocene.

4.1. *In situ ^{10}Be exposure ages*

The ^{10}Be ages for bench A are between 150.8 and 55.5 ka, with a mean age of 91.2 ± 30.9 ka for the seven samples. The mean age of the five effective samples (removing the outliers; Figs. 4A and 5A; Table 1) is further constrained to 86.4 ± 14.2 ka (range, 106.2 to 66.2 ka). We interpret that bench A was exposed during middle to late MIS 5 based on the ^{10}Be ages. The bench B sample ages are broadly scattered between 134.3 and 32.3 ka, with a mean age of 101.6 ± 37.9 ka for the six samples. One sample (JBG011) was removed as outlier, and the five effective samples were exposed between 134.3 and 87.7 ka, yielding a mean age at 115.5 ± 18.9 ka. These samples indicate that bench B was exposed throughout MIS 5. The ^{10}Be ages for bench C scattered between 267.9 and 52.6 ka, with a mean age of 155.4 ± 74.9 ka for the seven samples. Removing the three outliers, four effective samples have ^{10}Be age between 196.9 and 130.1 ka, yielding a mean age of 173.0 ± 30.7 ka. The ages scattered across multiple glacial/interglacial cycles (MIS 8–3 and MIS 7–5, respectively), some of the samples likely experienced prior exposure as older drift (Ivy-Ochs et al., 2007; Di Nicola et al., 2009).

The bench D sample ages range between 37.3 and 6.2 ka, with a mean age of 22.6 ± 11.4 ka for the eight samples. Seven of the samples are divided into strong bimodal distributions. One cluster ($n = 4$) is centered at 19.0–15.1 ka, with a mean age of 17.0 ± 2.0 ka, which are clearly fitted inner range of 2σ confidence level of SEM. The other cluster ($n = 3$) is centered at 37.3–32.6 ka, with a mean age of 35.4 ± 2.4 ka. These two clusters exhibit very high probabilities of late MIS 3 and late MIS 2 exposures, respectively (Fig. 4A). The bench E sample ages are broadly scattered between 56.1 and 7.9 ka, with a mean age of 19.9 ± 17.3 ka for the eight samples. Most of the samples ($n = 5$) are concentrated between 11.6 and 8.5 ka, yielding a mean age of 9.5 ± 1.6 ka. We interpret that bench E was exposed from the Early Holocene. Bench F, which is the lowest bench, exhibits the youngest ages, ranging from 7.9 to 4.5 ka, and yields a mean age of 6.1 ± 1.2 ka for the five samples (no outliers), which indicates exposure since the middle Holocene. Since the lower three benches (D–F) have tight and decisive clusters of ages, we only used the representative ages at these three benches in subsequent statistical analyses.

4.2. *^{10}Be/^{26}Al results*

We had difficulties in assigning the upper three benches (A–C) to specific timings of exposure, owing to the broad scatter in their exposure ages, especially for bench C. Therefore, we also analyzed the in situ ^{26}Al of the samples that were older than MIS 4 to determine whether they were continuously exposed (Lal, 1991; Gosse and Phillips, 2001). Reconstructing the exposure history of samples that are younger than MIS 4 is difficult, even via multi-isotope analysis (^{26}Al/^{10}Be), given the large error range. Only 6 of the 16 samples that yielded ^{10}Be/^{26}Al ratios are interpreted to record a simple exposure history (Fig. 4B; Table 2), with strong similar ages on MIS 5 exposures, centered on 100 ka, through whole three benches. Therefore, the samples with multiple exposures were ultimately excluded in interpreting the exposure age of each bench.

We obtained more probable ages at bench A by using the two samples with simple exposure histories. Each sample shows similar

Table 1
Result of ^{10}Be dating.

Name	Latitude (°S, DD)	Longitude (°E, DD)	Elevation (masl)	Thickness[a] (cm)	Shielding Factor[b]	Quartz[c] (g)	Be Carrier (g)	^{10}Be/^{9}Be[d,e] (10^{-13})	^{10}Be counts[e,f] (10^5 atoms g^{-1})	Exposure Age[e,g] (ka)
Bench A										
JBG001	74.59935	164.19303	314	6.1	0.999395	20.1269	0.4042	7.464 ± 0.176	9.873 ± 0.255	150.8 ± 13.0
JBG002	74.59935	164.19303	314	4.5	0.999395	20.0679	0.4101	4.253 ± 0.145	5.698 ± 0.205	84.5 ± 7.4
JBG003	74.59912	164.19902	302	6	0.999644	19.9982	0.4047	5.231 ± 0.151	6.954 ± 0.215	106.2 ± 9.2
JBG004	74.59912	164.19902	302	8	0.999644	20.0580	0.4020	4.208 ± 0.177	5.529 ± 0.242	85.4 ± 7.8
JBG005	74.59910	164.19925	301	7.5	0.999644	20.2405	0.4195	2.691 ± 0.118	3.634 ± 0.167	55.5 ± 5.1
JBG006	74.59910	164.19925	301	4.4	0.999644	20.0569	0.4105	3.314 ± 0.108	4.434 ± 0.154	66.2 ± 5.8
JBG007	74.59910	164.19925	301	5.1	0.999644	20.1609	0.4028	4.535 ± 0.139	5.945 ± 0.194	89.8 ± 7.8
Bench B										
JBG010	74.60113	164.20768	237	6	0.999494	20.2822	0.4064	4.116 ± 0.151	5.406 ± 0.209	87.7 ± 7.8
JBG011	74.60113	164.20768	237	5	0.999494	20.1995	0.3994	1.598 ± 0.097	2.035 ± 0.130	32.3 ± 3.3
JBG012	74.60135	164.20728	234	5.8	0.999494	20.4617	0.4043	5.713 ± 0.146	7.421 ± 0.206	121.6 ± 10.5
JBG013	74.60135	164.20728	234	5.2	0.999494	20.0710	0.4216	4.694 ± 0.125	6.471 ± 0.187	105.1 ± 9.0
JBG014	74.60135	164.20728	234	4.5	0.999494	19.9957	0.4083	5.895 ± 0.154	7.916 ± 0.224	128.6 ± 11.1
JBG015	74.60135	164.20728	234	4	0.999494	20.2210	0.3915	6.508 ± 0.151	8.292 ± 0.212	134.3 ± 11.5
Bench C										
JBG016	74.60595	164.20947	160	5.1	0.999100	20.0451	0.4278	7.813 ± 0.163	10.986 ± 0.256	196.9 ± 17.0
JBG017	74.60593	164.20958	160	4.4	0.999100	20.2418	0.4071	5.615 ± 0.197	7.424 ± 0.273	130.1 ± 11.7
JBG018	74.60602	164.20930	159	6.4	0.999100	20.0153	0.4000	8.107 ± 0.159	10.676 ± 0.237	193.4 ± 16.6
JBG019	74.60592	164.20927	160	6.1	0.999100	20.0700	0.3936	7.399 ± 0.165	9.557 ± 0.236	171.6 ± 14.8
JBG020	74.60603	164.20928	159	9.5	0.999100	20.0933	0.3925	10.985 ± 0.213	14.162 ± 0.310	267.9 ± 23.5
JBG021	74.60593	164.20597	157	7.6	0.999100	20.0051	0.4026	2.277 ± 0.096	2.976 ± 0.133	52.6 ± 4.8
JBG022	74.60600	164.20943	159	8	0.999100	20.1128	0.4142	3.139 ± 0.119	4.222 ± 0.169	75.2 ± 6.7
Bench D										
JBG023	74.61300	164.21878	90	5.4	0.999573	20.8411	0.3993	1.627 ± 0.085	2.008 ± 0.111	37.3 ± 3.6
JBG024	74.61298	164.21895	90	5.2	0.999573	20.0361	0.3984	0.686 ± 0.054	0.845 ± 0.073	15.5 ± 1.8
JBG025	74.61248	164.21983	90	7.1	0.999573	20.1602	0.4166	1.458 ± 0.074	1.934 ± 0.104	36.4 ± 3.5
JBG026	74.61242	164.22002	90	6.4	0.999573	20.2427	0.3997	0.303 ± 0.036	0.337 ± 0.050	6.2 ± 1.0
JBG027	74.61215	164.21983	90	6.2	0.999573	20.0802	0.3964	1.382 ± 0.070	1.748 ± 0.095	32.6 ± 3.1
JBG028	74.61225	164.22033	90	5.4	0.999573	20.0458	0.4000	0.825 ± 0.055	1.032 ± 0.075	19.0 ± 2.0
JBG029	74.61245	164.22013	90	4	0.999573	20.3301	0.4104	0.801 ± 0.055	1.011 ± 0.076	18.4 ± 2.0
JBG030	74.61263	164.22058	90	6.3	0.999573	20.7052	0.4474	0.613 ± 0.043	0.813 ± 0.064	15.1 ± 1.6
Bench E										
JBG031	74.61823	164.23032	41	10.4	0.999600	20.0597	0.3956	0.369 ± 0.035	0.424 ± 0.048	8.5 ± 1.1
JBG032	74.61823	164.23033	41	7.6	0.999600	20.1398	0.3905	0.358 ± 0.041	0.403 ± 0.055	7.9 ± 1.2
JBG033	74.61832	164.23027	41	5.2	0.999600	20.0004	0.3998	0.478 ± 0.043	0.573 ± 0.060	11.1 ± 1.4
JBG034	74.61832	164.23023	41	7.8	0.999600	20.2445	0.3902	0.505 ± 0.067	0.588 ± 0.087	11.6 ± 1.9
JBG035	74.61850	164.23015	41	8.8	0.999600	20.0869	0.3984	0.786 ± 0.059	0.974 ± 0.080	19.5 ± 2.2
JBG036	74.61857	164.23047	40	8.4	0.999600	20.1441	0.4170	2.073 ± 0.094	2.782 ± 0.133	56.1 ± 5.2
JBG037	74.61857	164.23037	40	7.4	0.999600	20.1129	0.4204	1.340 ± 0.074	1.794 ± 0.105	35.7 ± 3.5
JBG038	74.61857	164.23040	40	6.4	0.999600	20.0287	0.3934	0.378 ± 0.037	0.433 ± 0.050	8.4 ± 1.1
Bench F										
JBG039	74.62043	164.23302	33	5.5	0.999600	20.0163	0.4201	0.247 ± 0.034	0.280 ± 0.050	5.4 ± 1.0
JBG040	74.62043	164.23302	33	7.8	0.999600	20.3431	0.3981	0.221 ± 0.027	0.228 ± 0.038	4.5 ± 0.8
JBG041	74.62047	164.23322	33	7.2	0.999600	20.0630	0.3960	0.291 ± 0.033	0.322 ± 0.046	6.4 ± 1.0
JBG042	74.62047	164.23322	33	5.4	0.999600	20.1920	0.4311	0.331 ± 0.037	0.404 ± 0.056	7.9 ± 1.2
JBG043	74.62047	164.23312	33	6.4	0.999600	20.0253	0.4048	0.288 ± 0.033	0.325 ± 0.047	6.4 ± 1.0

[a] Thickness of erratic cobbles.
[b] Factors for correcting geometric shielding measured at 10° intervals.
[c] Density of granite (2.7 g cm^{-3}) was used.
[d] The ^{10}Be/^{9}Be ratios were normalized using 07KNSTD reference sample 5-1 (2.71E-11 ± 9.58E-14) of Nishiizumi et al. (2007) and ^{10}Be half-life of 1.38E6 (Korschinek et al., 2010).
[e] Uncertainties are calculated at the 1σ confidence level.
[f] A mean value of process blank samples (4.52E-15 ± 1.23E-15) was used for correction of background.
[g] Ages were calculated assuming zero erosion and using CRONUS-Earth online calculator 3.0 of Balco et al. (2008) with scaling factors of Stone (2000).

^{10}Be and ^{26}Al ages (106.2 and 98.5 ka; 85.4 and 78.9 ka) with little post-deglaciation processes. Mean age of simple exposures increased to 95.8 ± 14.7 ka (n = 2) from that of apparent whole samples (91.2 ± 30.9 ka; n = 7) and statistical inlier samples (86.4 ± 14.2 ka; n = 5), however still assigned to MIS 5. A MIS 6 outlier was also defined as a multiple-exposure sample. Bench B samples that are older than early MIS 5 were also identified as multiple-exposure samples. Two simple-exposure samples, with ages of 105.1 and 87.7 ka, yield an age range that is similar to the bench A exposure ages. Their mean age is 96.4 ± 12.3 ka, which is within uncertainly of the mean exposure age for bench A. Two simple exposure samples were obtained at bench C, but their exposure ages span MIS 5 (130.1 and 75.2 ka). The mean age of 102.7 ± 38.7 ka broadly falls within MIS 5, as do the ages for benches A and B.

5. Discussion

5.1. Timing of initial deglaciation at each bench

Our statistical evaluation documents that the two uppermost benches were exposed during MIS 5 (Fig. 5A; Tables 1 and 2). However, the scattered exposure ages, which span multiple glacial/interglacial cycles, are likely due to nuclide inheritances from pre-exposed bedrock fragments, older drift, and supraglacial erratics (Ivy-Ochs et al., 2007; Di Nicola et al., 2009). Our ^{10}Be/^{26}Al analysis

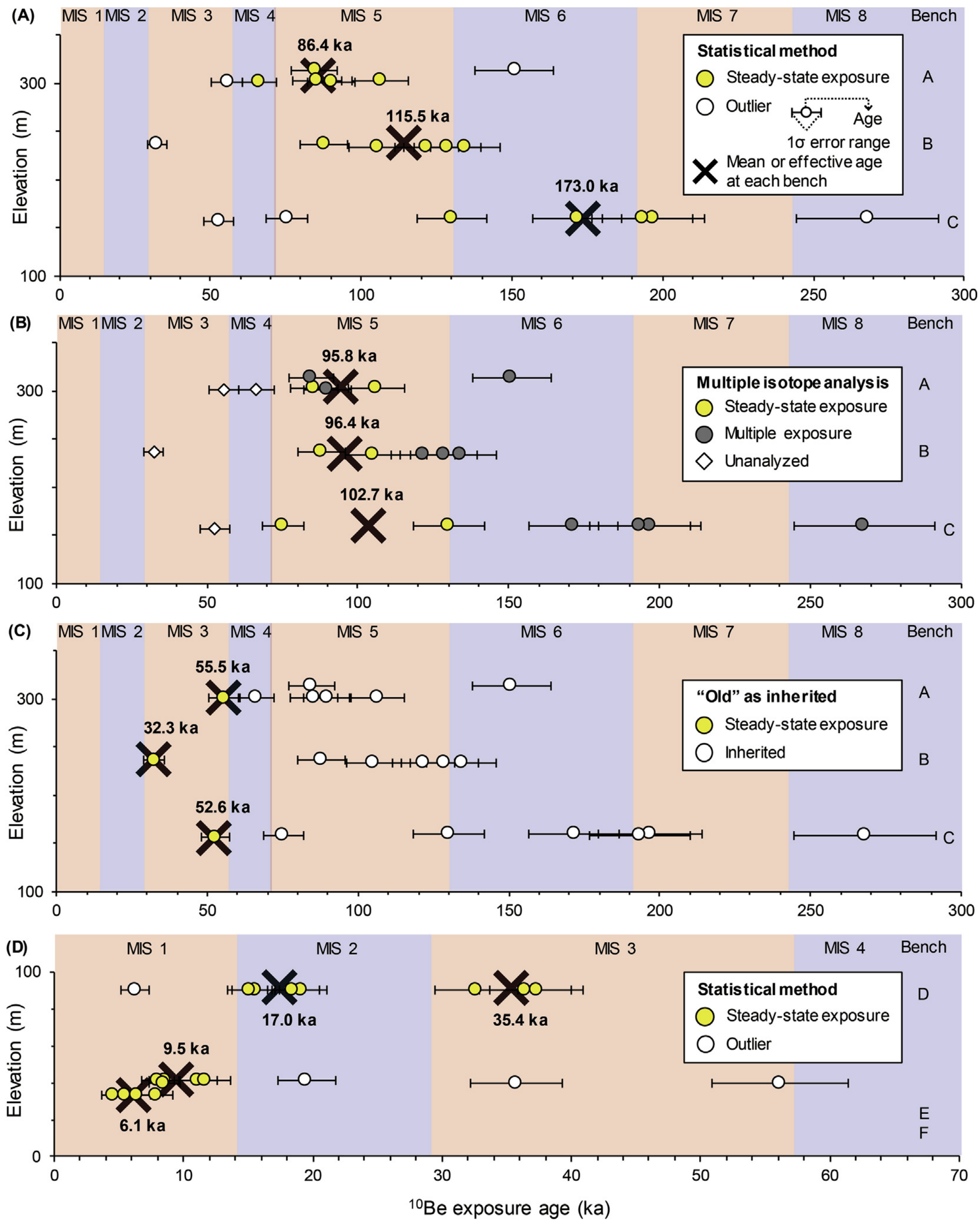

Fig. 5. The interpretative models for determining the effective ages of samples on upper three benches (benches A-C). (A) Statistical method with 95% confidence range. This method was rejected because it yields large scatter and inversed stratigraphy. (B) ^{10}Be exposure ages of the steady-state continuously exposed samples (yellow circles), combined with the ^{26}Al/^{10}Be ratios to reconstruct the exposure history (gray circles) and unanalyzed samples (white diamonds). We interpret this model is most reasonable because it accords to morphostratigraphy. (C) Taking youngest samples as true ages. Older samples are taken as outliers because they have inheritance. (D) The analytical results for determining the effective ages of lower three benches (benches D-F). (For interpretation of the references to colour in this figure legend, the reader is referred to the Web version of this article.)

at the upper three benches (A–C) indicate an MIS 5 exposure age (Fig. 5B; Tables 2 and 3). We adopted the single exposure ^{10}Be results for the three lower benches (D–F) (Fig. 5D; Table 3) because these benches yield concentrated clusters and there are inherent difficulties in employing ^{10}Be/^{26}Al analysis due to the young ages of these benches.

The age range obtained for bench A via multi-isotope analysis (Fig. 5B) indicates middle to late MIS 5 exposure, similar to the inlier results (106.2–85.4 ka) based on statistical method (Fig. 5A). We removed three older multiple-exposure samples from bench B, yielding a middle to late MIS 5 exposure (105.1–87.7 ka). The similar mean ages of benches A and B (95.8 ± 14.7 ka and 96.4 ± 12.2 ka, respectively) suggest that both benches were exposed at approximately the same time. Although only four samples from benches A and B yield simple exposure histories, we interpret that Campbell Glacier underwent rapid deglaciation from bench A to bench B during MIS 5. The two bench C samples with simple exposure histories are also centered on MIS 5 (102.7 ± 38.8 ka).

Several studies tried to find true deglaciation ages from

Table 2
Result of ^{10}Be and ^{26}Al dating.

Name	Elevation (masl)	Be[a] ^{10}Be counts (10^5 atoms g^{-1})	^{10}Be Exposure Age (ka)	Al ^{26}Al/^{27}Al[b,c] (10^{-13})	^{27}Al Conc.[d] (ppm)	^{26}Al counts (10^6 atoms g^{-1})	^{26}Al Exposure Age[e] (ka)	^{26}Al/^{10}Be[f]
Bench A								
JBG001	314	9.873 ± 0.255	150.8 ± 13.0	8.182 ± 0.648	25.37 ± 0.24	5.613 ± 0.445	125.2 ± 17.4	5.68 ± 0.45
JBG002	314	5.698 ± 0.205	84.5 ± 7.4	18.745 ± 1.190	7.11 ± 0.11	3.383 ± 0.212	72.6 ± 9.1	5.93 ± 0.37
JBG003	302	6.954 ± 0.215	106.2 ± 9.2	29.594 ± 1.081	5.92 ± 0.05	4.426 ± 0.161	98.5 ± 11.4	*6.36 ± 0.23*
JBG004	302	5.529 ± 0.242	85.4 ± 7.8	1.827 ± 0.294	74.83 ± 1.81	3.521 ± 0.566	78.9 ± 15.7	*6.37 ± 1.02*
JBG007	301	5.945 ± 0.194	89.8 ± 7.8	69.425 ± 6.251	1.55 ± 0.01	3.322 ± 0.252	72.5 ± 9.6	5.58 ± 0.42
Bench B								
JBG010	237	5.406 ± 0.209	87.7 ± 7.8	18.973 ± 0.895	6.84 ± 0.04	3.379 ± 0.169	79.5 ± 9.5	*6.25 ± 0.31*
JBG012	234	7.421 ± 0.206	121.6 ± 10.5	55.125 ± 4.068	2.47 ± 0.01	4.126 ± 0.264	98.1 ± 12.5	5.56 ± 0.35
JBG013	234	6.471 ± 0.187	105.1 ± 9.0	12.011 ± 0.799	11.79 ± 0.12	4.123 ± 0.266	97.5 ± 12.5	*6.37 ± 0.41*
JBG014	234	7.916 ± 0.224	128.6 ± 11.1	95.416 ± 9.003	1.44 ± 0.04	4.221 ± 0.342	99.4 ± 13.7	5.33 ± 0.43
JBG015	234	8.292 ± 0.212	134.3 ± 11.5	65.624 ± 2.164	2.49 ± 0.01	4.541 ± 0.149	106.9 ± 12.3	5.47 ± 0.18
Bench C								
JBG016	160	10.986 ± 0.256	196.9 ± 17.0	103.698 ± 6.265	2.06 ± 0.01	6.111 ± 0.369	160.7 ± 20.9	5.56 ± 0.33
JBG017	160	7.424 ± 0.273	130.1 ± 11.7	1.235 ± 0.231	169.80 ± 0.16	4.958 ± 0.972	127.6 ± 30.1	*6.67 ± 1.31*
JBG018	159	10.676 ± 0.237	193.4 ± 16.6	62.123 ± 2.387	2.94 ± 0.04	4.419 ± 0.169	115.0 ± 13.5	4.13 ± 0.15
JBG019	160	9.557 ± 0.236	171.6 ± 14.8	9.458 ± 0.829	19.42 ± 0.47	5.422 ± 0.475	142.5 ± 20.8	5.67 ± 0.49
JBG020	159	14.162 ± 0.310	267.9 ± 23.5	139.013 ± 5.797	1.82 ± 0.04	6.581 ± 0.274	181.3 ± 22.2	4.64 ± 0.19
JBG022	159	4.222 ± 0.169	75.2 ± 6.7	52.483 ± 17.494	2.14 ± 0.01	2.855 ± 0.499	73.8 ± 15.5	*6.76 ± 1.18*

[a] Note Table 1.
[b] Ratios of ^{26}Al/^{27}Al were normalized with KNSTD reference sample 4-1 (7.44E-11 ± 6.04E-13) of Nishiizumi et al. (2007).
[c] Uncertainties were calculated at the 1σ confidence level.
[d] Concentration of ^{27}Al was measured with ICP-AES from quartz dissolution aliquot.
[e] Ages were calculated assuming zero erosion with using CRONUS-Earth online calculator 3.0 of Balco et al. (2008).
[f] Italic values represent steady-state exposure samples (Fig. 4 B).

Table 3
Timing of initial exposure of each bench.

Bench	Elevation (m asl)	Apparent mean ages (with whole samples)				Apparent mean ages (outlier removed)		Steady state mean ages (^{10}Be/^{26}Al analysis)			Final assigned representative age	MIS
		n	^{10}Be age	n	^{26}Al age	n	^{10}Be age	n	^{10}Be age	^{26}Al age		
A	305	7	91.2 ± 30.9	5	89.5 ± 22.5	5	86.4 ± 14.2	2	95.8 ± 14.7	88.7 ± 13.8	95.8 ± 14.7	5
B	235	6	101.6 ± 37.9	5	96.3 ± 10.1	5	115.5 ± 18.9	2	96.4 ± 12.2	88.5 ± 12.7	96.4 ± 12.2	5
C	159	7	155.4 ± 74.9	6	133.5 ± 37.5	4	173.0 ± 30.7	2	102.7 ± 38.7	100.7 ± 38.0	102.7 ± 38.7	5
D	90	8	22.6 ± 11.4			4	17.0 ± 2.0				35.4 ± 2.4	3–2
						3	35.4 ± 2.4				~17.0 ± 2.0	
E	41	8	19.9 ± 17.3			5	9.5 ± 1.6				9.5 ± 1.6	1
F	33	5	6.1 ± 1.2			5	6.1 ± 1.2				6.1 ± 1.2	1

apparent exposure ages due to the scattered age spreads within a moraine group. A compilation study of thousands of erratic boulders' exposure ages revealed the oldest apparent ages should be taken as true deglaciation ages due to the critical problem of partial post-depositional shielding (Heyman et al., 2011). In contrary, the youngest ages were treated as true deglaciation ages when older samples in group have no significant inheritances (Owen et al., 2006). Among 20 samples from upper three benches (A-C), only four young samples (4/20) appeared on MIS 4 and 3, and the others (16/20) appeared over MIS 4. Ten inherited old samples (10/16) suggest the oldest apparent ages cannot represent the true deglaciation ages in our study area (Fig. 5B). Three youngest ages on each bench appeared on MIS 3, the similar period of prior exposure of bench D (Fig. 5C). However, the lowering rate of the glacier was not substantial, which is inconsistent with other climate proxies (Figs. 6 and 9; Discussion 5. 2.). Furthermore, six steady-state exposures (6/16) on MIS 5 show much stronger probability than those young ages and can be the true deglaciation ages (Fig. 5C). Those young outlier samples might have been derived by partial and temporal shielding of other erratics or matrix which could have made incomplete exposures. Those minor shielding matrix might have been transported out with heaving by annual freeze-thaw of snow.

Each of the simple exposure ages from the upper three benches (A–C; n = 6) indicates MIS 5 exposure (Fig. 5B). However, the samples that are likely older drifts with multiple-exposure histories discriminated in a plot of ^{10}Be–^{26}Al suggest two possible deglaciation scenarios: (1) continuous downwasting of Campbell Glacier from bench A to C occurred throughout MIS 5, continuing down to bench D; or (2) since the much older drifts only appeared at bench C, benches A and B were first exposed during MIS 5, followed by a potential minor glacier advance between benches B and C. Still they span on MIS 5 with centered on similar period with no younger evidence than bench B. We interpret that the first scenario would be more plausible which transported the older drift (e.g. JBG016, JBG018, JBG019, and JBG020) from upglacier regions because there is no sample older than MIS 5 at bench A and B (Fig. 5B).

Four of the eight samples from bench D are clustered at the range of 19.0–15.1 ka within the 2σ confidence level (Fig. 5D). Three of the other samples from bench D exhibit ages (37.3–32.6 ka) outside of this interval and yield a stronger probability density than the younger effective cluster. The mean ages, 35.4 ± 2.4 and 17.0 ± 2.0 ka, of these two clusters indicate exposures during late MIS 3 and at the end of MIS 2, respectively. The bimodal distribution of these strong probability density peaks ($p = 0.9396$ for the younger peak; $p = 0.9999$ for the older peak) suggests two different scenarios: (1) Campbell Glacier downwasted to bench D from its

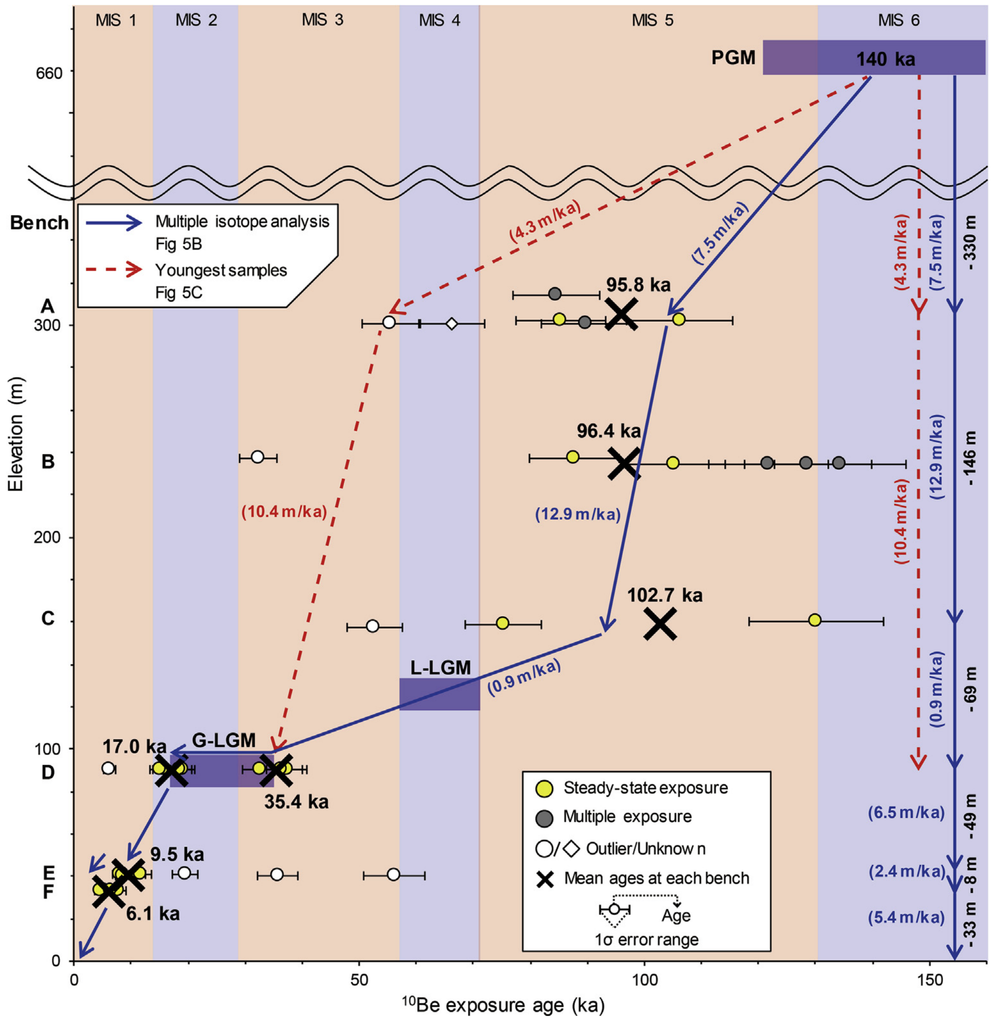

Fig. 6. Downwasting of Campbell Glacier from 140 ka to present. The purple boxes represent the timing of maximum extent of glacier ice elevation estimated by Di Nicola et al. (2009) and this study. Cases are divided into two periods for exposures of upper three benches. Blue arrows follow our final assignment with results of $^{26}Al/^{10}Be$ multiple isotope analysis (Fig. 5B). Red arrows follow youngest approach. The greatest lowering rate occurred during MIS 3 (Fig. 5C), which seems unrealistic based on the previous studies across the Antarctica. The crosses and bold numbers indicate the representative mean exposure age at each bench. The thickness and inferred lowering rate between each bench are provided to the right. (For interpretation of the references to colour in this figure legend, the reader is referred to the Web version of this article.)

earlier position at bench C and then reached an equilibrium at bench D from 35.4 ± 2.4 to 17.0 ± 2.0 ka; or (2) the samples with older exposures at 35.4 ± 2.4 ka might have been derived from a rockfall onto the glacier surface rather than subglacial quarrying, such that they were exposed at the surface for a long time before arriving at their present positions. We interpret the former scenario is more plausible, given the gentle slope (<5.4°) and lack of a local source area of mass movement, implying the older samples results from nuclide inheritances. The other two lower benches yield Early and Mid Holocene exposure ages. Bench E was exposed in the early Holocene (9.5 ± 1.6 ka) and bench F was exposed in the Mid Holocene (6.1 ± 1.2 ka), with constant lowering of the glacier between these two benches.

5.2. Dynamics of Campbell Glacier during the late Quaternary

The uppermost bench A (305 m asl) was completely covered by Campbell Glacier during the penultimate glacial period, MIS 6, and subsequently exposed during MIS 5 (95.8 ± 14.7 ka) (Figs. 6 and 7). Bench B (235 m asl) was initially exposed at a similar time (96.4 ± 12.2 ka), indicating rapid downwasting of Campbell Glacier by ~70 m. Deglaciation continued to bench C (159 m asl) during MIS 5, with another ~76 m of lowering (102.7 ± 38.7 ka). Campbell Glacier possibly experienced a minor advance during MIS 5, given the large scatter in exposure ages and much older drifts with complex exposure histories on bench C.

The decrease in exposure age of samples on benches A–C indicates that Campbell Glacier underwent rapid and extensive deglaciation prior to the beginning of the last glacial period. These benches have been continuously exposed since MIS 5, highlighting that Campbell Glacier reached its maximum thickness during the PGM in MIS 6, as opposed to the gLGM in MIS 2. This finding is also supported by the fact that no samples on the lower benches are older than MIS 3.

The exposure ages on benches C and D indicate that the ice dynamics of Campbell Glacier was dominated by deglaciation from the beginning of MIS 4 to the end of MIS 2, which continued throughout the last glacial period. The continuous downwasting of Campbell Glacier reached bench D (90 m asl) after a further ~69 m of lowering and exposed drifts between 17.0 ± 2.0 ka and 35.4 ± 2.4 ka. The latter timing of deglaciation is coincident with the A1 warming event recorded in the EPICA Dome C ice core (Jouzel et al.,

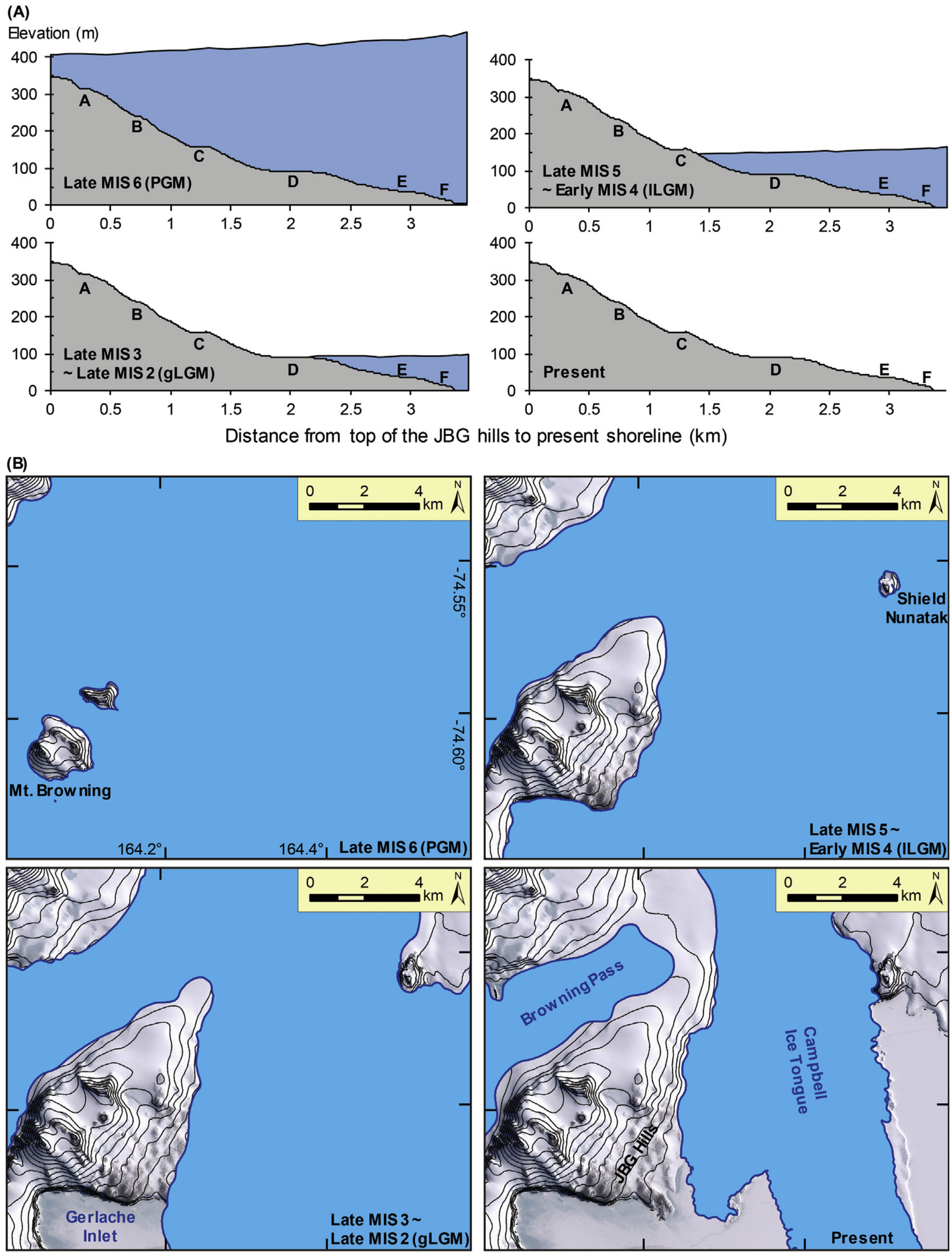

Fig. 7. (A) Longitudinal profiles showing the extent of Campbell Glacier across JBG Hills at each stage, indicated by the blue filled regions. (B) Estimated extent of Campbell Glacier at each stage, in plan view. (For interpretation of the references to colour in this figure legend, the reader is referred to the Web version of this article.)

2007). Penguin rookeries, which occur only in summertime ice-free areas of Cape Adare and Cape Hallet, have been dated to >35 and > 17.3 ka, respectively (Licht et al., 1996). Furthermore, the outer coastal region and inner bay of the Ross Sea show no evidence of expansion at the gLGM (Baroni and Orombelli, 1994).

The lack of older drifts and continuous downwasting suggest that Campbell Glacier was thicker during MIS 4, compared with MIS 2, during the last glacial cycle. The lLGM occurred at the beginning of MIS 4, immediately after MIS 5, with the extent of Campbell Glacier located right below bench C. The deglaciation continued to bench D, with a potential minor advance or stagnation at 35.4 ka, and the youngest erratics were exposed immediately after the gLGM during late MIS 2 (17.0 ka). Deglaciation continued to bench E (41 m asl), with ~49 m of thinning by 9.5 ± 1.6 ka, followed by a further ~8 m of lowering to bench F (33 m asl) by 6.1 ± 1.2 ka. The remainder of the slope (to 0 m asl) is now completely exposed.

In a study on Mt. Browning, 2 km from Jangbogo Hills, Di Nicola et al. (2009) reported that erratic boulders at 600–670 m asl were deposited during a glacier advance at ~140 ka. These authors analyzed ^{21}Ne, ^{10}Be, and ^{26}Al from erratic boulders and bedrock on

Mt. Browning and Mt. Abbott, with the intermediate ^{10}Be and ^{26}Al exposure ages of erratic boulders clustering at 140 ka, reflecting a glacial event. However, they could not fully discuss the glacial history of Campbell Glacier since the last glacial cycle because of the lack of samples and difficulties in evaluating multiple-exposure histories.

Our study provides a more detailed and plausible glacier history from the PGM to present. Campbell Glacier downwasted by ~330 m from the upper limit of the PGM to bench A between the PGM and middle MIS 5, at a lowering rate of 7.5 m ka^{-1} (Fig. 6). Intensive downwasting from bench A to C occurred during middle MIS 5, centered on 98.3 ± 19.6 ka, with ~150 m of lowering and the highest lowering rate (12.9 m ka^{-1}). The lowering rate between benches C and D, which occurred between the lLGM (MIS 4) and gLGM (MIS 2), decreased to 0.9 m ka^{-1}, with ~70 m of lowering. Several minor fluctuations (advances and/or stagnations) might have interrupted the otherwise continuous lowering during this period. The rate of ice lowering increased to 6.5 m ka^{-1} from the end of the gLGM (MIS 2) to the Holocene (MIS 1), with another ~50 m of lowering. It then decreased again to 2.4 m ka^{-1} between 9.5 and 6.1 ka, with a further ~10 m of lowering, which is coincident with the climatic optimum and rapid sea-level rise. It increased again during the late Holocene to 5.4 m ka^{-1}, with a final ~35 m of lowering to sea level. Based on the youngest samples (Fig. 5C), the highest lowering rate appeared during MIS 3 (10.4 m ka^{-1}) between bench A and D (Fig. 6). It was followed by slower downwasting down to bench A, from PGM to beginning of MIS 3 (4.3 m ka^{-1}). It is even still higher than the lowering rate during the Holocene (2.4–5.4 m ka^{-1}) which is not concordant with other climate proxies (Fig. 9).

5.3. Cenozoic glacier dynamics in Victoria Land

5.3.1. Middle Miocene–Early Pliocene glacier dynamics

We obtained systematically younger ages with decreasing elevation among the benches for the period from MIS 5 to the Holocene. There was no significant evidence of glacial advance that was extensive enough to rebury an exposed bench. Furthermore, the lack of young ages on the upper benches and lack of old ages on the lower benches highlight the deglaciation of Campbell Glacier as the dominant dynamic process over the last glacial cycle. Similar findings have been reported for this region, but other studies did not possess the evidence to confirm deglaciation within a million-year timescale (Nishiizumi et al., 1991; Ivy-Ochs et al., 1995; Schäfer et al., 1999; Di Nicola et al., 2012).

In a study across Allan Hills, Wright Valley, and Tillite Glacier in southern Victoria Land, Nishiizumi et al. (1991) suggested that there had been no ice sheet thickening in the region over the past several million years. Nishiizumi et al. (1991) collected bedrock samples and loose rock (ice-drifted) from the ice-free areas of the TAM, at the margin of the Ross Ice Shelf. They employed the same method as used in our study ($^{26}Al/^{10}Be$ cosmogenic nuclide ratios) and determined exposure ages of $\geq$3 Ma with very low erosion rates ($<10^{-5}$ cm a^{-1}), even though the samples were several tens of meters above the present ice surface. Ice-free areas located hundreds of meters above the present ice surface in the Dry Valleys also exhibit ^{10}Be ages at million-year timescales with extremely low erosion rates (Ivy-Ochs et al., 1995; Schäfer et al., 1999). These results indicate that the inner Dry Valleys were exposed at >6.5 Ma, with no landform changes (<15 cm Ma^{-1}) down to 870 m asl. Schäfer et al. (1999) also analyzed other nuclides (^{3}He and ^{20}Ne) to confirm the million-year timescales of the ^{10}Be ages, and found that these old exposures with low erosion rates were derived from a cold and hyperarid climate. A study on the Ricker Hills also indicated that an Early to Middle Pleistocene glacier was much thicker than it was in the late Pleistocene, with its ice surface being ~500 m higher than the current ice surface (Strasky et al., 2009).

Similar studies over long timescales have been conducted in northern Victoria Land, with comparable interpretations. The Antarctic tors or "Gargoyles" at Chisholm Hills, Mesa Range, are near the upglacier area of Campbell Glacier. These ice-free areas, which are 250 m above the present ice surface, have been continuously exposed for at least 3.5 Ma (Oberholzer et al., 2008). In a study at Black Ridge and Mt. Keinath in the Deep Freeze Range, Oberholzer et al. (2003) reported similar old exposures, low erosion rates, and a maximum glacial elevation during the Pleistocene. Oberholzer et al. (2003) analyzed ^{3}He, ^{10}Be, and ^{21}Ne in three morphological units and reported very old bedrock exposures (5.3 Ma, ~780 m above the present glacier surface), Older Drift (309 ka, 850 m asl), and Younger Drift (33.9 ka, 380 m above the present glacier surface). Mt. Pollock and Archambault Ridge in the upglacier area of Campbell Glacier have flat ice-free areas that were exposed prior to 7–5 Ma, with their relict landforms preserved due to extremely low erosion rates (~5 cm Ma^{-1}). These features are characteristic of a cold-based glacial environment that switched from a warm-based glacial environment during the middle Miocene (Di Nicola et al., 2012).

These studies revealed glacier dynamics at the million-year timescale from Pliocene/Pleistocene to present. The common interpretation is that the glaciers could not have reached their previous maxima during the last several million years. This similar pattern in the timing and mode of deglaciation might imply that both northern and southern Victoria Land has experienced a cold and hyperarid climate since the middle Pliocene (Oberholzer et al., 2003).

5.3.2. Late Pleistocene–Holocene glacier dynamics

An analysis of cosmogenic nuclides (^{10}Be, ^{21}Ne, and ^{26}Al) from the bedrock and erratic boulders on Mt. Abbott and Mt. Browning, the nearest locations to our study area, revealed 3.8 Ma bedrock exposures, as well as shorter timescale exposures (Ma, ka scale) from drifts or erratics (Di Nicola et al., 2009). The PGM occurred at ~140 ka at 600–670 m asl. The upper limits of ice coverage from each glacier drift has decreased continuously since the PGM along the slopes on the Northern Foothills. This decreasing pattern of drift elevation was also observed on Black Ridge and Mt. Keinath, following a similar trend during a similar period (Oberholzer et al., 2003). The same pattern is evident for Campbell Glacier, especially from MIS 6 to present.

The same pattern of decreasing drift elevation was observed at even shorter timescales on the nunataks at Grove Mountains in the interior East Antarctic Ice Sheet, based on erratics located several meters above the current glacier surface that were exposed as recently as 50 ka (Lilly et al., 2010). The simple exposures during the last glacial period, especially before the gLGM, suggest that ice was less extensive during the gLGM than during the lLGM at MIS 4. The same lLGM expansion on Denton Hills occurred at 36 ka and was more extensive than that during the gLGM (Joy et al., 2017). Furthermore, the lLGM at Denton Hills overlaps our bimodal age data of bench D, with pre-exposures at 35.4 ± 2.4 ka and a long stagnation to 17.0 ± 2.0 ka. Previous studies in Victoria Land failed to provide the full glacial history of the last glacial period due to a lack of samples for dating. Our study documents the timing and magnitude of lowering of glacier throughout the last glacial period (Figs. 6–8).

Rapid ice thinning during the post-gLGM period, primarily during the Holocene, has been studied mainly using cosmogenic exposure dating. For example, $^{26}Al/^{10}Be$ ages from Mac. Robertson Land, East Antarctica, indicate that the East Antarctic Ice Sheet has lost 350 m of ice since 13 ka (Mackintosh et al., 2007). Similar ice

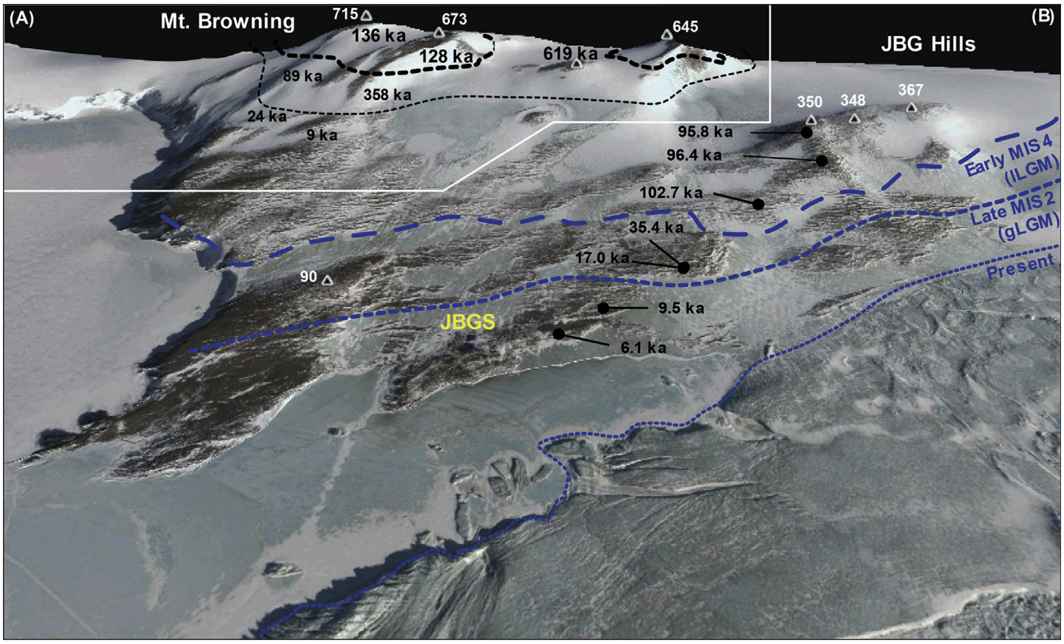

Fig. 8. Oblique view constructed with REMA (Referenced Elevation Model of Antarctica, 8-m resolution) data. The black triangles (with white values) denote peaks (with elevations). The black values from the ice-free areas are the ^{10}Be exposure ages at each bench in this study. (A) Previous study on Mt. Browning, Northern Foothills (Di Nicola et al., 2009). The dashed thick black lines indicate the upper limit of the Older Drift (early–middle Pleistocene), and the dotted black line indicates the upper limit of the Younger Drift (late Pleistocene). (B) JBG Hills, with the effective ages of each bench (ka). The blue lines indicate the estimated upper limit of Campbell Glacier at each period. JBGS is Jangbogo Station of Korea. (For interpretation of the references to colour in this figure legend, the reader is referred to the Web version of this article.)

thinning has been inferred on Tucker and Aviator glaciers, with thinning of 290–380 m and ≥250 m, respectively, since the gLGM (Goehring et al., 2019), assuming the lLGM occurred at MIS 2. Similar studies on the Antarctic Peninsula also suggested that the Holocene data are derived from gLGM ice extension, with subsequent exposure during the post-gLGM period (Balco and Schaefer, 2013; Jeong et al., 2018). These authors used the term LGM loosely to refer to the period of the last glacial-interglacial cycle, which is when the Antarctic ice sheets were near their maximum geographic extents, between approximately 25 and 15 ka. However, our data clearly indicate that the lLGM occurred during MIS 4, as opposed to MIS 2. We suggest that the glaciers in Victoria Land have experienced continuous surface lowering since the PGM, with no major glacier advance during the gLGM.

5.4. Climate signatures from erratics of Campbell Glacier and regional comparison

There are three well-studied ice cores from the Ross Sea region: Talos Dome, Taylor Dome, and Siple Dome (Fig. 9). The surface temperature data from Siple Dome show similar patterns to the δ^{18}O values from the other two domes in Victoria Land during the last 120 ka (Fig. 9B–D; Steig, 2006; Price et al., 2007; Bazin et al., 2013). These climate proxies correlate well with our probability density data of both the whole apparent ^{10}Be ages and steady-state ^{10}Be exposure ages (Fig. 9A) and lowering rate of the Campbell Glacier (Fig. 9B). The high probability density peaks of our exposure ages within the deglaciation periods correspond with periods of increasing surface temperatures (MIS 5, 3, and 1), and the three periods with limited relative exposure probability coincide with MIS 6, the lLGM (MIS 4), and the gLGM (early MIS 2) (Fig. 9A).

While the increased δ^{18}O values, temperatures, and CO_2 concentration during early MIS 5 drove high ablation rates and rapid deglaciation (Fig. 9D–F; Bazin et al., 2013; Köehler et al., 2017; Parrenin et al., 2013), our data suggest that much greater deglaciation occurred during middle to late MIS 5. The highest accumulation rate during early MIS 5 might have interrupted and overcome the strong ablation, resulting in lower melting rates than those inferred during middle to late MIS 5 (Figs. 6 and 9G; Vallelonga et al., 2013). Campbell Glacier underwent a rapid downwasting from its PGM elevation to bench A, with ~330 m of lowering. The maximum CO_2 concentration and high surface temperatures in the Antarctica intensified deglaciation during late MIS 5, which caused the greatest lowering rate of the ice surface in Jangbogo Hills from bench A to bench C (Fig. 9E and F; Hughes et al., 2013). The MIS 4 surface temperatures decreased with decreasing temperature from the beginning of the last glacial period. While these conditions favored weak ablation, accumulation also decreased due to the aridity and low snowfall. The surface temperature decrease during MIS 4 was comparable to that during MIS 2, but the snow accumulation rate was much higher during MIS 4. This combination of higher snow accumulation and similar ablation might have caused the lLGM to occur during MIS 4. Furthermore, the increased CO_2 concentration and surface temperatures might have interrupted the glacier advance due to increased ablation, with no major increase in snowfall during MIS 3. The reduced surface temperature and decreased snow accumulation during MIS 2 were followed by an abrupt increase in CO_2 concentration and surface temperatures at ~22 ka. Campbell Glacier continued to thin during MIS 2 at the lowest inferred lowering rate since the PGM, with no evidence of advancing over a previously exposed bench. Although the accumulation rate of snow and ice increased from late MIS 2, our data suggest that the deglaciation was dominant in the period. This negative mass balance could be derived by higher ablation with increased CO_2 and temperature, which exceeded the increased accumulation. However, the increased temperature already contributed its maximum effort to thinning of glacier during this period, and the sea level rise actually anticipated the retreat of glacier (Goehring et al., 2019). The reduced lowering rate of glacier between 9.5 and 6.1 ka also corresponds with the temporal

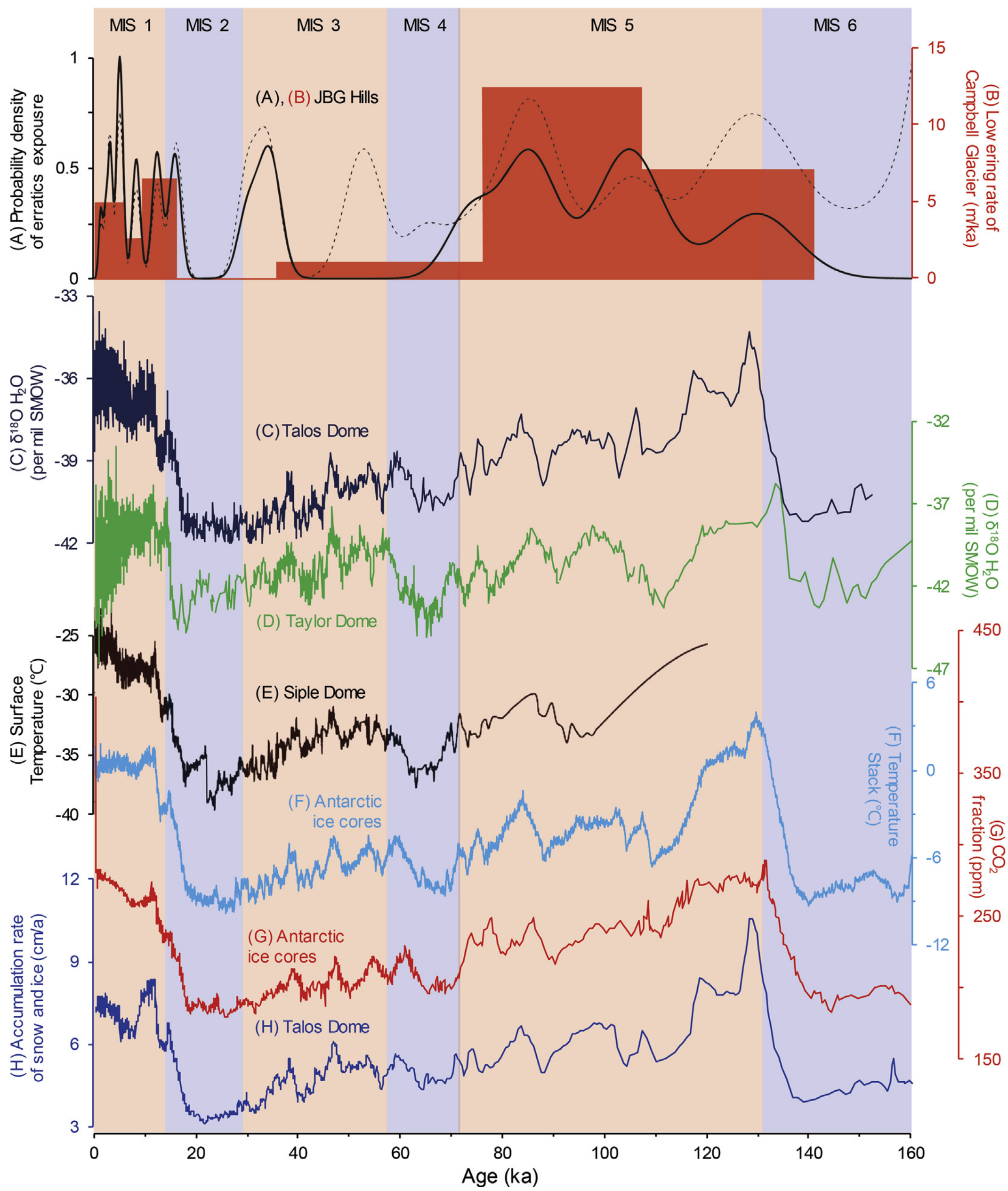

Fig. 9. Comparison of key Antarctic climate proxies and our exposure data. (A) Probability density curves for ^{10}Be exposure age data (this study). The dotted and solid lines are the whole apparent ^{10}Be ages and steady-state exposure ages, respectively. (B) Lowering rate changes of Campbell Glacier from 140 ka. (C) Talos Dome $\delta^{18}O$ H_2O values (Bazin et al., 2013). (D) Taylor Dome $\delta^{18}O$ H_2O values (Steig, 2006). (E) Siple Dome surface temperatures (Price et al., 2007). (F) Antarctic Temperature Stack (ATS) from five different ice cores (EDC, Vostok, Dome Fuji, TALDICE, and EDML) (Parrenin et al., 2013). (G) Continuous record of the atmospheric greenhouse gas carbon dioxide (CO_2) (Köehler et al., 2017) (H) Talos Dome accumulation rate of snow and ice (Vallelonga et al., 2013).

decrement of temperature proxies.

Many glaciers drain Victoria Land into TNB, with Taylor Dome and Talos Dome being the major drainage areas in southern and northern Victoria Land, respectively. Siple Dome is currently the primary drainage area in Marie Byrd Land that drains through the Ross Ice Shelf. Given the retreat records of the Ross Ice Shelf groundling line during the post-gLGM period (Halberstadt et al., 2016) and our finding that Campbell Glacier was thicker during MIS 4 than at the gLGM, the drainage systems of these three ice domes likely merged to form the Ross Ice Shelf sometime between the PGM and gLGM.

Deglaciation of the Ross Sea sector of Antarctica continued from the post-gLGM (~22 ka) to ~10 ka based on incrementally rising sea level and support of increasing temperature. Campbell Glacier lowered from bench D to bench E during this period, with an increased lowering rate similar to that inferred during early MIS 5. Snowfall and accumulation increased during early MIS 5, but they were overwhelmed by the rapid increase in surface temperature. Campbell Glacier continued to thin between 10 and 6 ka, but the glacier thickness was reduced by only a few meters. The continuous lowering of Campbell Glacier since the Holocene was driven by higher surface temperatures and decreased snow accumulation.

6. Conclusion

Previous surface-exposure dating studies of glacier landforms have contributed to the glacier histories of Victoria Land, Antarctica revealing the transition from warm-to cold-based glaciers on the basis of very old, glacially striated bedrock surfaces that have experienced minimal erosion. The glaciers in Victoria Land have experienced continuous lowering throughout the late Quaternary, with no abrupt increase in ice thickness beyond their earlier maximum positions. The observed million-year timescales of exposed bedrock suggest simple exposures without re-burial via glacier expansion. We also document decreasing ice thickness since MIS 6 over time at shorter cycles throughout the glacial/interglacial cycles from the penultimate glacial period to present.

Campbell Glacier reached its maximum thickness at ~140 ka (PGM) at ~630 m asl (Di Nicola et al., 2009), with largely continuous downwasting from MIS 6 to present. The glacier surface lowered to ~480 m asl during MIS 5 due to a large increase in surface temperature. Ice could not grow during the last glacial period due to decreased snowfall and low accumulation. Decreased surface temperatures kept ablation low during the last glacial period, but temperatures rose during MIS 3 and middle MIS 2, resulting in higher ablation than MIS 4. Campbell Glacier was thicker during the PGM than during the lLGM.

Campbell Glacier continued to thin during the last glacial period, with a potential minor stagnation on the same bench from MIS 3 to 2. The glacier reached its maximum thickness during the last glacial period at MIS 4 rather than at the gLGM (MIS 2). A combination of higher snowfall during MIS 4 and similar surface-temperature falls to those during MIS 2 produced more favorable conditions for glacier advancement. Campbell Glacier continued to lower throughout the Holocene, at a similar lowering rate to that during early MIS 5. This lowering rate was briefly interrupted during the middle Holocene but recovered its lowering momentum due to the rapid increase in surface temperature that continues today.

Acknowledgments

This research is supported by Korea Polar Research Institute (PE19030). We are greatly thankful to Dr. Lewis Owen for his help with improving the earlier version of the manuscript and two anonymous reviewers for their constructive comments. We were given lots of practical advice and unconditional support from Dr. Jong Ik Lee of Korea Polar Research Institute during the field trip. We would express sincere gratitude to him.

Appendix A. Supplementary data

Supplementary data to this article can be found online at https://doi.org/10.1016/j.quascirev.2019.105897.

References

Balco, G., Schaefer, J.M., LARISSA Group, 2013. Exposure-age record of Holocene ice sheet and ice shelf change in the northeast Antarctic Peninsula. Quat. Sci. Rev. 59, 101–111.
Balco, G., Stone, J.O., Lifton, N.A., Dunai, T.J., 2008. A complete and easily accessible means of calculating surface exposure ages or erosion rates from 10Be and 26Al measurements. Quat. Geochronol. 3 (3), 174–195.
Baroni, C., Noti, V., Ciccacci, S., Righini, G., Salvatore, M.C., 2005. Fluvial origin of the valley system in northern Victoria Land (Antarctica) from quantitative geomorphic analysis. Geol. Soc. Am. Bull. 117 (1–2), 212–228.
Baroni, C., Orombelli, G., 1994. Holocene glacier variations in the Terra Nova bay area (Victoria Land, Antarctica). Antarct. Sci. 6 (4), 497–505.
Bazin, L., Landais, A., Lemieux-Dudon, B., Toyé Mahamadou Kele, H., Veres, D., Parrenin, F., Martinerie, P., Ritz, C., Capron, E., Lipenkov, V.Y., Loutre, M.F., Raynaud, D., Vinther, B.M., Svensson, A.M., Rasmussen, S.,O., Severi, M., Blunier, T., Leuenberger, M.C., Fischer, H., Masson-Delmotte, V., Chappellaz, J.A., Wolff, E.W., 2013. Delta 18O measured on ice core TALDICE on AICC2012 chronology. PANGAEA. https://doi.org/10.1594/PANGAEA.824890.
Clark, P.U., Dyke, A.S., Shakun, J.D., Carlson, A.E., Clark, J., Wohlfarth, B., Mitrovica, J.X., Hostetler, S.W., McCabe, A.M., 2009. The last glacial maximum. Science 325 (5941), 710–714.
CLIMAP Project, 1981. Seasonal Reconstructions of the Earth's Surface at the Last Glacial Maximum. Geological Society of America, Map and Chart Series, p. 18. MC-36.
Di Nicola, L., Baroni, C., Strasky, S., Salvatore, M.C., Schlüchter, C., Akçar, N., Kubik, P.W., Wieler, R., 2012. Multiple cosmogenic nuclides document the stability of the East Antarctic ice sheet in northern Victoria Land since the late Miocene (5–7 Ma). Quat. Sci. Rev. 57, 85–94.
Di Nicola, L., Strasky, S., Schlüchter, C., Salvatore, M.C., Akçar, N., Kubik, P.W., Christl, M., Kasper, H.U., Wieler, R., Baroni, C., 2009. Multiple cosmogenic nuclides document complex Pleistocene exposure history of glacial drifts in Terra Nova Bay (northern Victoria Land, Antarctica). Quat. Res. 71 (1), 83–92.
Douglas, Curran-Everett, 2008. Explorations in statistics: standard deviations and standard errors. Adv. Physiol. Educ. 32 (3), 203–208.
Fabel, D., Harbor, J., 1999. The use of in-situ produced cosmogenic radionuclides in glaciology and glacial geomorphology. Ann. Glaciol. 28, 103–110.
Goehring, B.M., Balco, G., Todd, C., Moening-Swanson, I., Nichols, K., 2019. Late-glacial grounding line retreat in the northern Ross Sea, Antarctica. Geology 47 (4), 291–294.
Gosse, J.C., Phillips, F.M., 2001. Terrestrial in situ cosmogenic nuclides: theory and application. Quat. Sci. Rev. 20 (14), 1475–1560.
Halberstadt, A.R.W., Simkins, L.M., Greenwood, S.L., Anderson, J.B., 2016. Past ice-sheet behaviour: retreat scenarios and changing controls in the Ross Sea, Antarctica. Cryosphere 10, 1003–1020.
Han, S.W., Ahn, J.W., Kim, Y.J., 2017. Overwintering Report of the Antarctic Jang Bogo Station 3rd Overwintering Party. Korea Polar Research Institute, pp. 125–160.
Heyman, J., Stroeven, A.P., Harbor, J.M., Caffee, M.W., 2011. Too young or too old: evaluating cosmogenic exposure dating based on an analysis of compiled boulder exposure ages. Earth Planet. Sci. Lett. 302, 71–80.
Howat, I.M., Porter, C., Smith, B.E., Noh, M.-J., Morin, P., 2019. The reference elevation model of Antarctica. Cryosphere 13, 665–674.
Hughes, P.D., Gibbard, P.L., Ehlers, J., 2013. Timing of glaciation during the last glacial cycle: evaluating the concept of a global 'Last Glacial Maximum'(LGM). Earth Sci. Rev. 125, 171–198.
Ivy-Ochs, S., Kerschner, H., Schlüchter, C., 2007. Cosmogenic nuclides and the dating of Lateglacial and Early Holocene glacier variations: the Alpine perspective. Quat. Int. 164, 53–63.
Ivy-Ochs, S., Schlüchter, C., Kubik, P.W., Dittrich-Hannen, B., Beer, J., 1995. Minimum ^{10}Be exposure ages of early Pliocene for the table mountain plateau and the Sirius group at mount Fleming, dry valleys, Antarctica. Geology 23 (11), 1007–1010.
Jeong, A., Lee, J.I., Seong, Y.B., Balco, G., Yoo, K.C., Yoon, H.I., Domack, E., Rhee, H.H., Yu, B.Y., 2018. Late Quaternary deglacial history across the Larsen B embayment, Antarctica. Quat. Sci. Rev. 189, 134–148.
Jouzel, J., Stievenard, M., Johnsen, S.J., Landais, A., Masson-Delmotte, V., Sveinbjornsdottir, A., Vimeux, F., Von Grafenstein, U., White, J.W., 2007. The GRIP deuterium-excess record. Quat. Sci. Rev. 26 (1–2), 1–17.
Joy, K., Fink, D., Storey, B., De Pascale, G.P., Quigley, M., Fujioka, T., 2017. Cosmogenic evidence for limited local LGM glacial expansion, Denton Hills, Antarctica. Quat. Sci. Rev. 178, 89–101.
Kim, H.C., Kim, D.Y., Lee, J.I., Woo, J.S., Koh, H.J., Lee, S.R., 2018. Geologic Map Around the Jang Bogo Station, Northern Victoria Land, Antarctica. 1:20,000. Project publication of the Korea Polar Research Institute and Ministry of Ocean and Fisheries, Republic of Korea.
Kohl, C.P., Nishiizumi, K., 1992. Chemical isolation of quartz for measurement of in-situ-produced cosmogenic nuclides. Geochem. Cosmochim. Acta 56 (9), 3583–3587.
Köehler, P., Nehrbass-Ahles, C., Schmitt, J., Stocker, T.F., Fischer, H., 2017. Continuous record of the atmospheric greenhouse gas carbon dioxide (CO2), raw data. PANGAEA. https://doi.org/10.1594/PANGAEA.871265.
Korschinek, G., Bergmaier, A., Faestermann, T., Gerstmann, U.C., Knie, K., Rugel, G., Wallner, A., Dillmann, I., Dollinger, G., Von Gostomski, C.L., Kossert, K., 2010. A new value for the half-life of 10Be by heavy-ion elastic recoil detection and liquid scintillation counting. Nucl. Instrum. Methods Phys. Res. Sect. B Beam Interact. Mater. Atoms 268 (2), 187–191.
Lal, D., 1991. Cosmic ray labeling of erosion surfaces: in situ nuclide production rates and erosion models. Earth Planet. Sci. Lett. 104 (2–4), 424–439.
Licht, K.J., Jennings, A.E., Andrews, J.T., Williams, K.M., 1996. Chronology of late Wisconsin ice retreat from the western Ross sea, Antarctica. Geology 24, 223–226.
Lilly, K., Fink, D., Fabel, D., Lambeck, K., 2010. Pleistocene dynamics of the interior East Antarctic ice sheet. Geology 38 (8), 703–706.
Mackintosh, A., White, D., Fink, D., Gore, D.B., Pickard, J., Fanning, P.C., 2007. Exposure ages from mountain dipsticks in Mac. Robertson Land, East Antarctica, indicate little change in ice-sheet thickness since the Last Glacial maximum. Geology 35 (6), 551–554.
Nishiizumi, K., Imamura, M., Caffee, M.W., Southon, J.R., Finkel, R.C., McAninch, J., 2007. Absolute calibration of 10Be AMS standards. Nucl. Instrum. Methods Phys. Res. Sect. B Beam Interact. Mater. Atoms 258 (2), 403–413.
Nishiizumi, K., Kohl, C.P., Arnold, J.R., Klein, J., Fink, D., Middleton, R., 1991. Cosmic ray produced 10Be and 26Al in Antarctic rocks: exposure and erosion history. Earth Planet. Sci. Lett. 104 (2–4), 440–454.
Oberholzer, P., Baroni, C., Salvatore, M.C., Baur, H., Wieler, R., 2008. Dating late Cenozoic erosional surfaces in Victoria Land, Antarctica, with cosmogenic neon in pyroxenes. Antarct. Sci. 20 (1), 89–98.

Oberholzer, P., Baroni, C., Schaefer, J.M., Orombelli, G., Ochs, S.I., Kubik, P.W., Baur, H., Wieler, R., 2003. Limited Pliocene/pleistocene glaciation in Deep freeze range, northern Victoria Land, Antarctica, derived from in situ cosmogenic nuclides. Antarct. Sci. 15 (4), 493–502.
Owen, L.A., Caffee, M.W., Bovard, K.R., Finkel, R.C., Sharma, M.C., 2006. Terrestrial cosmogenic nuclide surface exposure dating of the oldest glacial successions in the Himalayan orogen: Ladakh Range, northern India. GSA Bull. 118 (3–4), 383–392.
Parrenin, F., Masson-Delmotte, V., Köehler, P., Raynaud, D., Paillard, D., Schwander, J., Barbante, C., Landais, A., Wegner, A., Jouzel, J., 2013. Antarctic temperature Stack (ATS) from five different ice cores (EDC, Vostok, dome Fuji, TALDICE, and EDML). PANGAEA. https://doi.org/10.1594/PANGAEA.810188.
Price, S.F., Conway, H., Waddington, E.D., 2007. Evidence for late pleistocene thinning of Siple dome, west Antarctica. J. Geophys. Res.: Earth Surf. 112, F03021.
Rohling, E.J., Hibbert, F.D., Williams, F.H., Grant, K.M., Marino, G., Foster, G.L., Hennekam, R., De Lange, G.J., Roberts, A.P., Yu, J., Webster, J.M., 2017. Differences between the last two glacial maxima and implications for ice-sheet, δ18O, and sea-level reconstructions. Quat. Sci. Rev. 176, 1–28.
Schäfer, J.M., Ivy-Ochs, S., Wieler, R., Leya, I., Baur, H., Denton, G.H., Schlüchter, C., 1999. Cosmogenic noble gas studies in the oldest landscape on earth: surface exposure ages of the Dry Valleys, Antarctica. Earth Planet. Sci. Lett. 167 (3–4), 215–226.
Seong, Y.B., Dorn, R.I., Yu, B.Y., 2016. Evaluating the life expectancy of a desert pavement. Earth Sci. Rev. 162, 129–154.
Smith, J.A., Seltzer, G.O., Farber, D.L., Rodbell, D.T., Finkel, R.C., 2005. Early local last glacial maximum in the tropical Andes. Science 308 (5722), 678–681.
Steig, Eric J., 2006. High resolution stable isotopes of ice core Taylor Dome to 230 kyr. PANGAEA. https://doi.org/10.1594/PANGAEA.472831.
Stone, J.O., 2000. Air pressure and cosmogenic isotope production. J. Geophys. Res.: Solid Earth 105 (B10), 23753–23759.
Strasky, S., Di Nicola, L., Baroni, C., Salvatore, M.C., Baur, H., Kubik, P.W., Schlüchter, C., Wieler, R., 2009. Surface exposure ages imply multiple low-amplitude Pleistocene variations in East Antarctic ice sheet, Ricker Hills, Victoria Land. Antarct. Sci. 21 (1), 59–69.
Vallelonga, P.T., Barbante, C., Cozzi, G., Gabrieli, J., Schüpbach, S., Spolaor, A., Turetta, C., 2013. Iron (Fe) concentrations and fluxes in TALDICE ice core 0.6 to 314 ky BP. PANGAEA. https://doi.org/10.1594/PANGAEA.808940.